APPENDIX

1. Membrane binding constants

Unit conversions for concentrations of proteins from molar to μm^{-2} membranes:

$$[F_o] = [F'_o]/(120 \times [C'])$$

Where $[F_o]$ and $[F'_o]$ are initial LukF concentrations applied to cells in μm^{-2} and M, respectively. 120 μm^2 is the membrane area of one erythrocyte. $[C']$ is the cell concentration in M (6×10^{10} cells/l = 0.1 pM). The same definition was also applied to $[F_b]$ which is the concentration of membrane-bound LukF.

Membrane binding constants for each component (K_F and K_H in μm^2) were calculated as follows:

$$K_F = [F_b] \times ([F_o] - [F_b])^{-1} \times (R_F - [F_b])^{-1}$$

where R_F is concentration of binding sites for LukF in μm^{-2}. The above calculation was also applied to HS.

2. Association constants

$K_{F\cdot H}$, $K_{F2\cdot H1}$, $K_{F1\cdot H2}$, $K_{(F\cdot H)2}$, $K_{F3\cdot H3-4}(K_p)$, K_{2p}, K_{3p}, K_{4p} (μm^2) were estimated based on concentrations of intermediates at equilibrium. For example,

$$K_{F\cdot H} = [F\cdot H] \times [F_1]^{-1} \times [H_1]^{-1} \text{ or}$$
$$K_p = [F_3\cdot H_{3-4}] \times [(F\cdot H)_2]^{-1} \times [F\cdot H]^{-1}$$

where $[F_1]$ and $[H_1]$ (μm^{-2}) were measured by dividing the total fluorescence intensity by the intensity of single monomers. $[F\cdot H]$, $[(F\cdot H)_2]$, $[F_3\cdot H_{3-4}]$, $[F_6\cdot H_{6-8}]$, $[F_9\cdot H_{9-12}]$ and $[F_{12}\cdot H_{12-16}]$ are numbers of dimers, tetramers, single pores, two pores, three pores and four pores per μm^2, estimated based on the FRET-IC5 intensity spots corresponding to 1, 2, 3, 6, 9 and 12 times $I_{FRET\text{-}IC5}$. $[F_1]$ and $[H_1]$ were corrected by subtracting the number of LukF or HS assembled into oligomers from the previously measured values.

3. Theoretical distribution of intermediates at certain protein concentrations

Basic equations for each intermediate are presented given approximations of $[F_b] << R_F$ and $[H_b] << R_H$ as follows (Oosawa and Kasai, 1962):

$$[F_s] = [F_1]/(K_F \times R_F); [H_s] = [H_1]/(K_H \times R_H)$$

$$[D_1] = K_1 \times [F_1] \times [H_1];$$

$$[D_2] = K_2 \times [D_1]^2$$

$$[D_3] \text{ or } [P_1] = K_p \times K_2 \times [D_1]^3$$

$$[P_n] = K_{2p} \times K_{np}^{n-2} \times [D_3]^n;\ n = 2, 3, 4...$$

$$[F_0] = [F_s] + [F_b] = [F_s] + [F_1] + \sum_{n=1}^{3} \times [D_n] + \sum_{n=2}^{\infty} n \times [P_n]$$

$$[H_0] = [H_s] + [H_b] = [H_s] + [H_1] + \sum_{n=1}^{3} n \times [D_n] + \sum_{n=2}^{\infty} 3n \times [P_n]$$

where $[F_s]$ is the concentration of unbound protein in solution ($[F_0] - [F_1]$), D_1 and D_2 are shorthand for $F\cdot H$ and $(F\cdot H)_2$, respectively. The theoretical values shown in Figures 2B and 6A were calculated using KaleidaGraph. The definition for each intermediate is as described in Table I and Figure 6B.

Coordination of kinesin's two heads studied with mutant heterodimers

Kuniyoshi Kaseda*†, Hideo Higuchi‡, and Keiko Hirose*§

*Gene Function Research Laboratory, National Institute of Advanced Industrial Science and Technology, and †Japan Society for the Promotion of Science, 1-1-1 Higashi, Tsukuba, Ibaraki 305-8562, Japan; and ‡Department of Metallurgy, Graduate School of Engineering and Center for Interdisciplinary Research, Tohoku University, Sendai, Miyagi 980-8579, Japan

Edited by Clara Franzini-Armstrong, University of Pennsylvania School of Medicine, Philadelphia, PA, and approved October 22, 2002 (received for review July 10, 2002)

A conventional kinesin molecule has two identical catalytic domains (heads) and is thought to use them alternately to move processively, with 8-nm steps. To clarify how each head contributes to the observed steps, we have constructed heterodimeric kinesins that consist of two distinct heads. The heterodimers in which one of the heads is mutated in a microtubule-binding loop moved processively, even when the parent mutant homodimers bound too weakly to retain microtubules in microtubule-gliding assays. The velocities of the heterodimers were only slightly higher than those of the mutant homodimers, although mixtures of these weak-binding mutant homodimers and the WT dimers moved microtubules at a velocity similar to the WT. Thus, the mutant head affects the motility of the WT head only when they are in the same molecule. The maximum force a single heterodimer produced in optical trapping nanometry was intermediate between the WT and mutant homodimers, indicating that both heads contribute to the maximum force at the same time. These results demonstrate close collaboration of kinesin's two heads in producing force and motility.

A conventional kinesin molecule is a homodimer with two catalytic domains (heads) linked together by a coiled-coil, and can move continuously for hundreds of steps along a microtubule (MT) track (1–3). Although monomeric constructs of kinesin can support MT movement in *in vitro* assays, various lines of evidence have shown that the two-headed structure is important for motility of conventional kinesins. For example, the velocities of monomeric constructs of kinesin are considerably slower than those of dimers (4, 5). Heterodimeric kinesin that lacks one of the two heads (one-headed kinesin) also showed much-decreased MT-gliding velocities (6). In addition, these monomeric or one-headed kinesins showed little or no processivity (4, 5, 7).

To move processively without dissociating from a MT, at least one of the heads is always bound to a MT. For a dimeric kinesin to stay bound to a MT, it is thought that the two heads of a kinesin coordinate their mechanochemical cycles. Previous biochemical studies have indicated the existence of functionally significant coordination between the two heads (8–12). For example, ATP binding by one of the heads triggers ADP release from the other (8–10). Also, the ATPase rate of one-headed kinesin dimers was decreased by almost 10-fold compared with that of two-headed kinesins (11). However, a large part of the mechanism for coordination is still unknown.

With the two heads, kinesin can move continuously for hundreds of nanometers against an applied load. Previous optical trapping experiments have shown that a kinesin dimer moves with discrete steps of 8 nm and can produce force up to several piconewtons (13–16). However, it is not yet known how each of the two heads contributes to the observed force. Comparing the force with that produced by monomeric or one-headed kinesins is also difficult, because monomeric or one-headed kinesins tend to detach from a MT before producing enough force to be measured.

One of the difficulties in studying the roles of each head in force production and motility comes from the fact that the two heads are identical, so that we cannot distinguish the contribution of one head from the other. To circumvent this problem, we have constructed heterodimeric kinesins that consist of two distinct motor domains. Using heterodimers in which one of the heads is mutated, we measured the velocities and the maximum force a single heterodimer produces and compared them with those of the WT and mutant homodimers. The results indicated close collaboration of kinesin's two heads in force production and motility.

Materials and Methods

Expression Constructs. Heterodimeric kinesins were prepared by coexpressing the WT and mutant K432 (a construct of human conventional kinesin consisting of amino acid residues 1–432), tagged with GST and histidine residues, respectively. First, a pET17b vector (Novagen) containing K432 with a C-terminal eight-histidine sequence (K432-His/pET17b) was made by using a K560-His construct in a pET17b vector (K560-His/pET17b) (17) as a starting material. A DNA fragment encoding K432 with an *Eco*RI site, the stop codon, and a *Xho*I site at the 3′ end was amplified by PCR and digested with *Sac*I and *Xho*I. The resulting fragment, encoding amino acid residues 366–432, was subcloned into K560-His/pET17b digested by the same two restriction enzymes to produce K432/pET17b. An oligonucleotide encoding consecutive histidine residues was introduced into the *Eco*RI site of K432/pET17b. Thus prepared K432-His/pET17b encodes the heavy chain B (51 kDa) as shown in Fig. 1*a*.

A plasmid encoding K432 with an N-terminal GST tag was also prepared by subcloning K432 in a vector carrying GST (pGEX-2T). A DNA fragment encoding the entire sequence of K432 was excised from K432/pET17b by digestion with *Nde*I and *Xho*I, rendered blunt with the Klenow fragment, and subcloned into the *Sma*I site of pGEX-2T (18). To use the same promoters for both K432-His and GST-K432 of a heterodimer, a T7 promoter was substituted for the *tac* promoter of pGEX-2T. The resulting construct, K432/pGEX-2T, encodes the heavy chain A (77 kDa) in Fig. 1*a*.

A series of mutant kinesins was prepared by using K432-His/pET17b by QuikChange mutagenesis (Stratagene). To produce the L11 mutant, the codons for K240, L248, and K252 in K432-His/pET17b were all mutated to those for alanine residues. The L12 (Y274A/R278A/K281A), L8 (E158A/K159A/R161A), and L13 (G291A/G292A) mutants were similarly prepared. To obtain heterodimeric kinesins, DNA fragments encoding the WT and mutated kinesins were placed side by side in a vector (Fig. 1*a*). In brief, K432-His/pET17b-based plasmids were digested by *Bgl*II, followed by a Klenow fragment treat-

This paper was submitted directly (Track II) to the PNAS office.

Abbreviations: K432, a construct of human conventional kinesin consisting of amino acid residues 1–432; MT, microtubule.

§To whom correspondence should be addressed. E-mail: k.hirose@aist.go.jp.

www.pnas.org/cgi/doi/10.1073/pnas.252409199

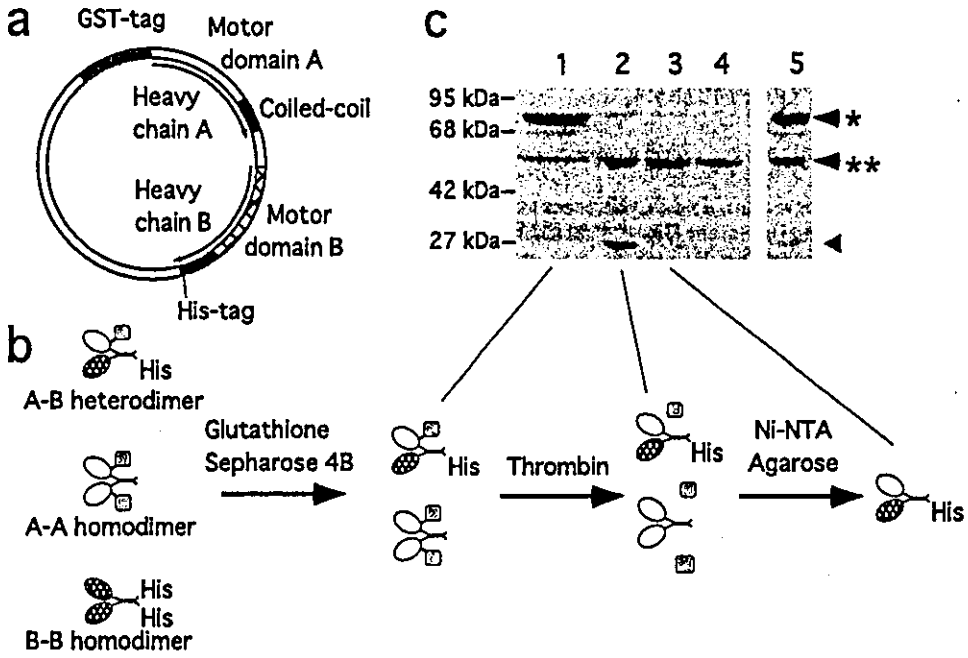

Fig. 1. Purification of heterodimeric kinesin. (*a*) Coexpression vector for generating heterodimeric kinesin. The two heavy chains in a kinesin heterodimer contain distinct motor domains attached to two different carrier sequences. The DNA fragments encoding the heavy chains A and B are placed side by side in a pGEX-2T-based vector. (*b*) The strategy for purifying heterodimeric kinesin. Three kinds of dimeric kinesins (A-B heterodimer, A-A homodimer, and B-B homodimer) form spontaneously via the coiled-coil regions. The heterodimeric kinesin with two different tags is separated from the homodimeric kinesins with two identical tags by the two-step affinity purification. (*c*) The SDS/PAGE patterns during the purification of WT/WT-His, after purification with glutathione Sepharose 4B/glutathione (lane 1), digestion by thrombin (lane 2), purification with Ni-NTA agarose/imidazole (lane 3), and removal of residual GST and GST-tagged protein with glutathione beads (lane 4). Lane 5 shows the WT dimer prepared by the same method but without digestion of GST (GST-WT/WT-His). The positions of K432 with a GST-tag and with a His-tag are indicated by an asterisk and double asterisks, respectively, and the cleaved GST is indicated by an arrowhead.

ment. After digestion by *Aat*II, the fragments were introduced into K432/pGEX-2T treated by *Bsa*AI/*Aat*II. All PCR products and mutations were checked by DNA sequencing.

Protein Expression and Purification. Proteins were expressed in BLR (DE3) pLys S (Novagen) freshly transformed with the plasmids (17). After being washed with buffer A (10 mM Tris-acetate, pH 8.0/4 mM magnesium acetate/250 mM potassium acetate/0.05% 2-mercaptoethanol), the bacterial cells were resuspended in buffer A supplemented with 1 mM ATP and protease inhibitors (17), disrupted by sonication, and then centrifuged (30,000 × *g*, 30 min).

To separate heterodimeric kinesins from other species, two-step affinity purification was performed (Fig. 1*b*). First, 1/40 volume of Glutathione 4B Sepharose resin (Amersham Pharmacia) was incubated with the supernatant on a roller for 1–2 h. The beads were collected by brief centrifugation (30 s at 500 × *g*) and washed with buffer A. The proteins were eluted with 20 mM glutathione (Fig. 1*c*, lane 1), and dialyzed against buffer A. GST was then removed by a treatment with 5 units/ml thrombin (Sigma) for 2–6 h in the presence of 2 mM $CaCl_2$ (Fig. 1*c*, lane 2). To collect the heterodimers, 1/20 volume of Ni-NTA agarose resin (Qiagen, Chatsworth, CA) was incubated with the resultant solution for 1–2 h. The beads were washed with buffer A containing 30 mM imidazole, and the proteins were eluted by applying 200 mM imidazole to the beads (Fig. 1*c*, lane 3). Finally, to remove a trace of residual GST-tagged kinesin and GST, Glutathione 4B Sepharose beads were incubated with the protein solution for 30 min, and centrifuged briefly. The supernatant was then concentrated (Fig. 1*c*, lane 4), and aliquots were stored in liquid nitrogen. To avoid loss of activity, the protein was kept at 4°C and in 100 μM ATP at all times. All of the mutant dimers were prepared and assayed in parallel with the WT kinesin. The histidine-tagged homodimeric kinesins were purified by using the Ni-NTA agarose/imidazole procedure. The concentration of the protein was determined by the Bradford method (19). Native PAGE was performed at pH 8 (20).

ATPase Assay. Steady-state MT-stimulated ATPase rates were measured by using malachite green (21). The motors (typically 40–200 nM) and MTs (0.1–50 μM tubulin dimers) were mixed at 27 ± 0.1°C in 10 mM Tris-acetate, pH 7.5/2 mM Mg-acetate/1 mM EGTA/1 mM Mg-ATP/20 μM paclitaxel. The ATPase assay was repeated three to six times with at least two different kinesin preparations. The ATPase data were fit to the Michaelis–Menten equation to determine the K_m(MT) and k_{cat} values.

Multiple Motor Motility Assay. A Penta-His Antibody (Qiagen) was fixed on the nitrocellulose-coated surface of a coverslip. The chamber was washed with 1 mg/ml BSA to remove the unbound antibody and then filled with 25 mg/ml BSA. The histidine-tagged kinesin (0.05–3 μM) was added into the flow chamber. After removal of unbound kinesin, tetramethylrhodamine-labeled MTs were introduced. Finally, the chamber was filled with the assay buffer [10 mM Tris-acetate, pH 7.5/4 mM Mg-acetate/50 mM K-acetate/1 mM EGTA/20 μM paclitaxel/0.5 mg/ml casein/0.5% 2-mercaptoethanol/1 mM ATP, and the oxygen scavenger system (22) at 25 ± 1 or 30 ± 1°C]. MTs were visualized under a fluorescent microscope equipped with a silicon-intensified target (SIT) camera (C2400-08; Hamamatsu Photonics, Hamamatsu City, Japan). Two to four independent batches of protein preparation were analyzed for each construct.

Optical Trapping Nanometry. The apparatus of trapping nanometry was as described (23). For specific attachment to latex beads, a sequence for biotinylation was added at the C terminus of heavy

chain A (Fig. 1*a*) (24). The oligonucleotides encoding a sequence LGSIFEAQKIEWR (25), which is biotinylated in *Escherichia coli*, was introduced into the *Eco*RI site of K432/pGEX-2T. The biotinylated kinesins, purified as described above, were incubated with streptavidin-coated 0.2-μm beads for >20 min at 25 ± 1°C. After tetramethylrhodamine-labeled MTs were bound directly to a coverslip, a kinesin-coated bead was placed in contact with a MT by using an optical trap. The displacement of kinesin was corrected by multiplying the factor $[(K_t + K_p)/K_p]$ to the observed bead displacement, where K_t and K_p are the stiffness of the optical trap and the stiffness of bead-to-glass linkage, respectively (13, 26). The total stiffness ($K_t + K_p$) and the trap stiffness K_t were determined by using the equipartition method from the Brownian noise of the bead movement (13, 27). After high-pass filtering at 10 Hz, the SD values were calculated at every 0.1 s of individual traces, grouped according to bead displacement, and averaged to determine the stiffness ($K_t + K_p$) at given displacement values. The range of the correction factor used was 1.1–1.7.

The experiments were performed in 80 mM Pipes, pH 6.8/2 mM $MgCl_2$/1 mM EGTA/1 mM ATP, and an oxygen scavenging system (22), at 24–26°C. The concentration of kinesin (5–50 nM, unless indicated otherwise) was determined so that the probability of the kinesin-coated beads to move on a MT was 0.15–0.35. Under this condition, it is considered that only a single kinesin molecule is involved in the movement of a bead (14, 26). To investigate the force–velocity relationships, the velocities were calculated at several points in the time course of the displacement as in Fig. 4*a*, from the slope of the trace. The force–velocity data sets from different traces were grouped according to the force. At every 0.5 pN (for the WT) or 0.15 pN (for the mutant), the velocity and force were averaged within the group. The averaged velocities were plotted against the averaged force.

Results and Discussion

Preparation of Heterodimeric Kinesins. We have produced heterodimeric kinesins, which possess two distinct heads, by coexpressing the WT and mutant kinesin heavy chains attached to different tags: consecutive histidine residues (His) and GST (Fig. 1*a*). Heterodimers (A-B heterodimer in Fig. 1*b*) were separated from other species (A-A and B-B homodimers), first by using Glutathione Sepharose 4B, then with Ni-NTA agarose, and further purified with glutathione beads. Thus purified heterodimeric kinesin appeared as a single band by SDS/PAGE/Coomassie Brilliant blue staining (Fig. 1*c*, lane 4), because the A and B heavy chains after removal of GST have similar molecular weights. When GST was not removed, the SDS gel showed two bands (Fig. 1*c*, lane 5), corresponding to the heavy chain A attached to GST (marked by an asterisk) and the heavy chain B with histidine residues (double asterisks). Densitometry of the gel showed that these heavy chains are present in a proportion of one to one. The results indicate that the purified protein is indeed heterodimeric, and that there is no detectable contamination by homodimers.

We have also examined the possibility of recombination that might occur after the purification; native PAGE patterns of the WT dimer prepared as above without removal of GST (GST-WT/WT-His) were compared with those of the GST-WT homodimer and WT-His homodimer. The mobility of GST-WT/WT-His was intermediate between the GST-WT and WT-His homodimers, and the patterns did not change for at least 4 h after the proteins were thawed (data not shown). The native PAGE pattern of WT/WT-His (prepared by thrombin-digestion of GST-WT/WT-His) also remained constant, and there was no band corresponding to monomers that would form in the process of recombination. Because all our measurements were started immediately after the protein was thawed and finished within 2 h, contamination by recombination, if any, was negligible. Typically, heterodimeric proteins of 0.03–0.1 mg were obtained per liter of culture.

To confirm that the expression and purification using these two different tags does not affect the functions of the motors, we prepared the WT kinesin dimers by the above method (WT/WT-His) and compared their biochemical properties with those of the dimers expressed with His-tags only (WT-His/WT-His). The observed K_m(MT), k_{cat}, and the MT-gliding velocities of WT/WT-His were similar to those of WT-His/WT-His (Table 1), and were also in agreement with previous work (4).

Table 1. Summary of ATPase measurement, MT-gliding assays, and single-molecule experiments of the homodimeric and heterodimeric kinesin constructs

		ATPase assay		Gliding assay	Beads assay
	Construct	k_{cat} (s^{-1}·head^{-1})	K_m(MT), μM	Velocity, nm/s	Stall force, pN
Homodimer	WT*	28.3 ± 2.5	0.4 ± 0.2	679 ± 59	6.3 ± 0.9
	WT†	27.8 ± 1.7	0.5 ± 0.2	683 ± 42	6.0 ± 0.3
	L11/L11	11.1 ± 1.2	1.1 ± 0.3	179 ± 23	1.0 ± 0.2
	L12/L12	0.8‡	ND‡	0§	0§
	L8/L8	20.8 ± 3.1	1.2 ± 0.6	514 ± 31	4.0 ± 0.5
	L13/L13	19.8 ± 2.0	0.3 ± 0.2	5 ± 1	0¶
Heterodimer	WT/L11	20.2 ± 1.7	1.0 ± 0.3	202 ± 29	1.8 ± 0.3
	WT/L12	16.6 ± 2.2	2.0 ± 0.4	101 ± 25	0.8 ± 0.2
	WT/L8	22.7 ± 1.4	0.5 ± 0.2	554 ± 29	6.0 ± 0.7
	WT/L13	24.1 ± 0.7	0.2 ± 0.1	8 ± 1	0¶

The values of k_{cat}, K_m(MT), the gliding velocity, and the stall force are shown as the mean ± SD. The stall force was determined from the level of the plateau of the traces as shown in Fig. 3. ND, not determined.

*WT kinesin homodimers with His-tags (WT-His/WT-His).

†WT kinesin homodimers prepared with two different tags (WT/WT-His). The stall force of WT/WT-His was measured by using 1.0-μm beads.

‡The k_{cat} and K_m(MT) of L12/L12 could not be accurately measured because of low affinity to MTs. The indicated value is the ATPase rate with 50 μM tubulin.

§In the gliding assay, the L12/L12 homodimers did not retain MTs. In the beads assay, attachment signals were observed only when they exist in excess, but no movement was detected.

¶These constructs did not show processive behavior at a single-molecule level, although the beads moved continuously when more than one molecule was bound.

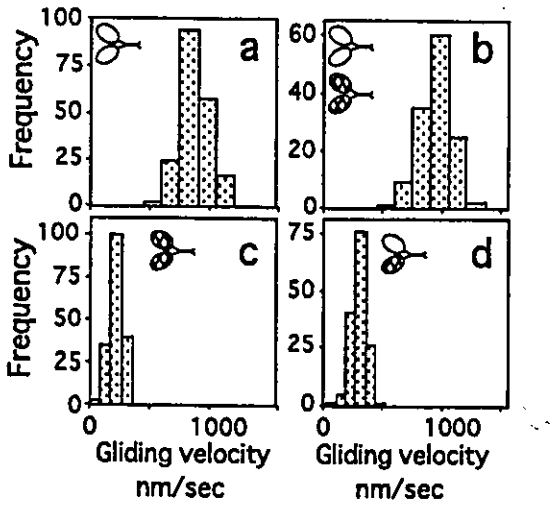

Fig. 2. Histograms of MT-gliding velocities of the WT and L11 mutant kinesins. The assay chambers were coated with the WT kinesin (*a*), the wild-type and L11/L11 homodimers mixed in a proportion of 1:1 (*b*), L11/L11 homodimers (*c*), and WT/L11 heterodimers (*d*). The gliding velocity of the L11/L11 was much lower than the WT, but the copresence of L11/L11 did not interfere with the motility of MTs on the WT kinesin homodimers. The gliding velocity of WT/L11 was only slightly higher than that of L11/L11 homodimers. These assays were performed at 30 ± 1°C, so that the velocities were higher than the values obtained at 25 ± 1°C, as in Table 1.

Mutations Used for Making Heterodimeric Kinesins. Using this method, we made heterodimeric kinesins in which one of the two heads is altered in the functions of either MT binding ["L11" (K240A/L248A/K252A), "L12" (Y274A/R278A/K281A), and "L8" (E158A/K159A/R161A)] or mechanochemical coupling ["L13" (G291A/G292A)]. The residues to be mutated were chosen according to the previous reports by using alanine scanning and proteolysis experiments (4, 28, 29). In agreement with them, the homodimers of the first three mutants showed higher K_m values, lower k_{cat}, and slower MT gliding (Table 1, Fig. 2*c*). Of these, the homodimers of the L12 mutant were reported to have neither measurable MT-activated ATPase nor MT-gliding activity (28). In our case also, MTs did not bind to the L12/L12-coated glass surface in multiple-motor-gliding assays, even in the absence of nucleotides. On the other hand, L11/L11 and L8/L8 supported MT gliding, with velocities that are 26% and 76% of the WT homodimers, respectively. The homodimer of the uncoupling mutant, L13/L13, was previously shown to have almost normal MT-activated ATPase, but the MT-gliding velocity decreased by ~100-fold (4). Our results were consistent with the report (Table 1).

Mixing Experiments of the WT and Mutant Homodimers. Using the L11/L11 and L12/L12 homodimers, we have also examined the MT-gliding activity caused by a mixture of the WT and mutated kinesin homodimers. When the wild-type and L11/L11 homodimers were introduced into an assay chamber in a proportion of 1:1 (Fig. 2*b*), the averaged MT-gliding velocities were comparable with the velocity driven by the WT alone (Fig. 2*a*). Similar results were obtained with mixtures of the WT and L12/L12 homodimers (data not shown). These results show that the copresence of the L11/L11 or L12/L12 homodimers, which bind only weakly to MTs, do not interfere with the motility of the MTs supported by the WT homodimers.

ATPase Activities and MT-Gliding Velocities of the Heterodimers. In contrast to the experiments using mixtures of homodimers, the MT-gliding velocities of the WT/L11 and WT/L12 heterodimers were considerably slower than that of the WT (Fig. 2*d*, Table 1). The percentages of the velocities relative to the WT homodimer are shown in Fig. 3. The average velocity of WT/L11 (202 ± 29 nm/s, n = 20; 30% of WT) was only slightly higher than that of L11/L11 (179 ± 23 nm/s, n = 14; 26% of WT). Although the L12/L12 homodimers did not retain MTs at the glass surface, WT/L12 was found to move MTs at 15% of the velocity of the WT (101 ± 25 nm/s, n = 16). Thus, mutant heads, when they exist as homodimers, did not slow down the movement of MTs supported by the WT homodimers but did cause a decrease in the velocity when they formed heterodimers with WT heads. The MT-gliding velocities of WT/L8 and WT/L13 were also significantly slower than the WT (Table 1, Fig. 3). The results indicate that a kinesin head needs a proper partner to produce normal velocity; the two heads must be closely cooperating in determining the velocity.

The ATPase rates of the heterodimers were intermediate between the WT and the parent mutant homodimers (Table 1, Fig. 3). For example, k_{cat} of L11/WT was 20.2 ± 1.7 ATP/s/head, which was approximately equal to the average of the WT and L11 homodimers [(28.3 + 11.1)/2 = 19.7]. Other heterodimers also showed k_{cat} values close to the average of the parent homodimers, suggesting that the maximum MT-activated ATPase rate of each head in a heterodimer is similar to that in a homodimer. To confirm the results, we made a heterodimer in which one of the heads is mutated so that it cannot hydrolyze ATP (E236A in ref. 30). The observed k_{cat} of the heterodimer WT/E236A (12.9 ± 1.7 ATP/s/head) was ~1/2 of the WT homodimer, confirming that the ATPase activity of each head was not largely affected by its partner head.

These results indicate that the two heads of a heterodimer have different ATPase rates. It is difficult to explain by a simple form of hand-over-hand models, in which the two heads of a kinesin hydrolyze ATP alternately. Another unexpected result was that, although the L11/WT, L12/WT, and L13/WT het-

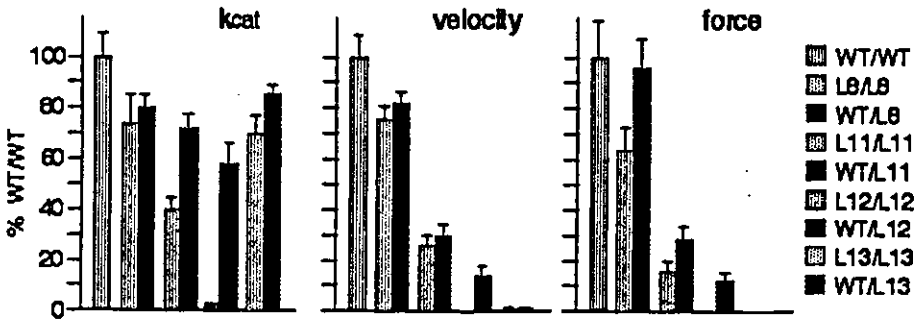

Fig. 3. The maximum MT-activated ATPase rates, the MT-gliding velocities, and the maximum forces of the homodimeric and heterodimeric kinesin constructs. Percentages relative to those of the WT homodimer are shown.

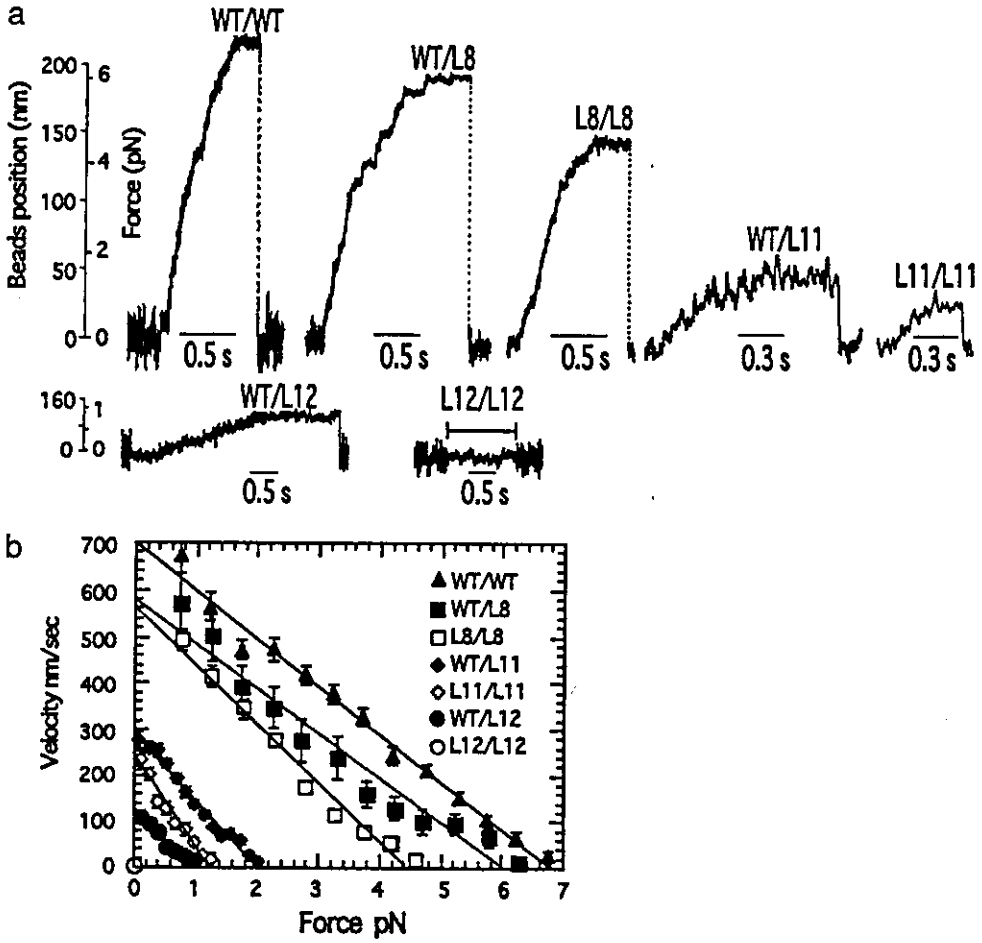

Fig. 4. Optical trapping nanometry for measurement of stall force. (*a*) Representative traces of the displacement of kinesin-coated beads along a MT. The displacement of the bead and the corresponding force are indicated on the left. For WT/L12 and L12/L12, the scale of displacement is different, because a weaker trap stiffness was used (0.007 pN/nm, instead of 0.032 pN/nm used for others). Applied force is shown on the same scale but the time scale is different in each trace. In the case of L12/L12, a higher concentration of kinesin (1–2 μM instead of 5–50 nM) was needed to observe any attachment signals (reduced vibration, as indicated by the solid line). In this case, more than one molecule is expected to be involved. (*b*) The force–velocity relationships of the WT kinesin (black, filled triangle), WT/L8 (blue, filled square), L8/L8 (blue, open square), WT/L11 (green, filled diamond), L11/L11 (green, open diamond), WT/L12 (red, filled circle), and L12/L12 (red, open circle). Solid lines represent the best fit of the data, and the *y* axis and *x* axis show the maximum velocity and the stall force, respectively.

erodimers showed k_{cat} values >50% of the WT homodimer, their velocities were only ~30, 20, and 1% of the WT homodimer, respectively (Fig. 3). These results are inconsistent with tightly coupled models, in which each ATP hydrolysis leads to an 8-nm step. We think that a proper coordination of the two heads was disrupted in heterodimers, which caused futile ATPase cycles.

The gliding speed of WT/L11 did not change as the surface density of the heterodimer was varied, similar to the case of the WT (data not shown). At a very low surface density of WT/L11, some MTs exhibited thermally driven pivot motions around a single contact point on the glass surface at which a single heterodimer is presumably located (31), while gliding slowly. The averaged gliding velocity of such MTs was in good agreement with the speed induced by multiple motors (271 ± 39 nm/s and 283 ± 33 nm/s at 30°C, for single and multiple motors, respectively; these velocities are higher than those in Table 1, which were measured at 25°C). The results suggest that a WT/L11 heterodimer can move processively along a MT, even though the mutant head may have only a weak affinity for MTs. Surprisingly, the WT/L12 heterodimer showed the same processive feature, even though the L12/L12 homodimers did not retain MTs at the glass surface. The average gliding speed of these MTs, presumably supported by a single molecule of WT/L12, was again similar to that of multiple motors.

Optical Trapping Nanometry. Processive movement of the WT/L11, WT/L12, and WT/L8 heterodimers was confirmed in optical trapping experiments. When 0.2-μm beads were coated with a low density of kinesin at which only a single kinesin dimer per bead is thought to interact with a MT (see *Materials and Methods*), these three heterodimers, as well as the L11/L11 and L8/L8 homodimers, moved the beads (Fig. 4*a*). In the force–velocity curve (Fig. 4*b*), the velocity decreased almost linearly with increasing force. The maximum velocities of the heterodimers estimated from the force–velocity curve were in agreement with those measured in the multiple motor assays, confirming that their velocities do not depend on the number of motors. As expected, L12/L12 exhibited no signal at a single molecule level. At a higher density of L12/L12, the beads sometimes appeared to attach to the MT (indicated by a solid line in Fig. 4*a*), but no significant movement was observed. Hancock and Howard (6) reported that a heterodimeric kinesin that lacks one of the heads cannot move processively. The processive movement of the WT/L12 heterodimer suggests that even a mutant head that has only a weak affinity to MTs can help its partner WT head to move the molecule processively. With the L13/L13 homodimer and WT/L13 heterodimer, the bead bound briefly to a MT but did not show processive movement at a single molecule level.

With the WT and L8/L8 homodimers and the WT/L8 heterodimer, many beads moved continuously until they stalled before detaching from the MT (Fig. 4*a*). The averaged stall force exerted by a WT homodimer (6.3 ± 0.9 pN, $n = 35$; Table 1), determined from the level of the plateau of the traces, was similar to those previously reported using single, native kinesin molecules and recombinant kinesins (13–16). The stall force of L8/L8 (4.0 ± 0.5 pN, $n = 22$) was smaller than the WT. Although the distance moved was shorter for WT/L11, WT/L12, and L11/L11 than for the WT, enough beads moved continuously until they reached the maximum force to determine the stall force. As expected from these experiments, L11/L11 showed a considerably smaller stall force (1.0 ± 0.2 pN, $n = 36$) than the WT. The heterodimers WT/L11, WT/L12, and WT/L8 showed the stall forces that are intermediate between the WT and mutant homodimers [1.8 ± 0.3 pN ($n = 74$), 0.8 ± 0.2 pN ($n = 29$), and 6.0 ± 0.7 pN ($n = 18$), for WT/L11, WT/L12, and WT/L8, respectively]. These values were in agreement with the stall forces obtained from the force–velocity curve in Fig. 4*b*.

It is not known which process during the kinesin's mechanical and chemical cycle determines the stall force, although it was reported that it does not depend on the temperature (32) or the concentration of ATP (13). If each head of a dimer is alternately and independently responsible for producing force, we might expect the stall force of a heterodimer to be determined by the weaker of the two heads, i.e., the mutant. However, the observed stall forces were significantly larger than those of the mutant homodimers ($P < 0.005$, t test). The results indicate that both heads of a dimer must cooperate in producing the maximum force.

Conclusion

In the present work, we have succeeded in generating heterodimeric kinesins in which one of the two heads was mutated. The resulting heterodimers moved processively, even when the mutant head had only a weak affinity to a MT. This is in contrast to a one-headed dimer, which did not move processively (6). Use of processive heterodimeric kinesins enabled us to measure the force and velocity produced by a single heterodimer and thus investigate the contribution of each head in force production and motility. Our results indicated a close mechanical cooperation of the two heads: a head cannot produce the maximum force and velocity by itself. The results are supported by previous biochemical studies showing that the two heads communicate with each other (8–12). In the most generally accepted model, a kinesin dimer uses the two heads alternately, moving in a hand-over-hand fashion (8–12, 33–36). In contrast, there are other models in which one of the heads is always leading (37). In the former case, however, the time interval between successive 8-nm steps (dwell time) in heterodimers should be different every other time. With a statistical analysis of the dwell time, our method of using heterodimeric kinesins opens the way to test alternate stepping models directly.

We thank Drs. L. A. Amos, T. Q. P. Uyeda, and Y. Hiratsuka for helpful comments on the manuscript and other colleagues for valuable discussion and technical advice. This work was aided by support from the Human Frontier Science Program and Japan Society for the Promotion of Science.

1. Howard, J., Hudspeth, A. J. & Vale, R. D. (1989) *Nature* **342**, 154–158.
2. Block, S. M., Goldstein, L. S. & Schnapp, B. J. (1990) *Nature* **348**, 348–352.
3. Vale, R. D., Funatsu, T., Pierce, D. W., Romberg, L., Harada, Y. & Yanagida, T. (1996) *Nature* **380**, 451–453.
4. Case, R. B., Rice, S., Hart, C. L., Ly, B. & Vale, R. D. (2000) *Curr. Biol.* **10**, 157–160.
5. Inoue, Y., Iwane, A. H., Miyai, T., Muto, E. & Yanagida, T. (2001) *Biophys. J.* **81**, 2838–2850.
6. Hancock, W. O. & Howard, J. (1998) *J. Cell Biol.* **140**, 1396–1405.
7. Berliner, E., Young, E. C., Anderson, K., Mahtani, H. K. & Gelles, J. (1995) *Nature* **373**, 718–721.
8. Hackney, D. D. (1994) *Proc. Natl. Acad. Sci. USA* **91**, 6865–6869.
9. Gilbert, S. P., Moyer, M. L. & Johnson, K. A. (1998) *Biochemistry* **37**, 792–799.
10. Ma, Y. Z. & Taylor, E. W. (1997) *J. Biol. Chem.* **272**, 724–730.
11. Hancock, W. O. & Howard, J. (1999) *Proc. Natl. Acad. Sci. USA* **96**, 13147–13152.
12. Crevel, I., Carter, N., Schliwa, M. & Cross R. (1999) *EMBO J.* **18**, 5863–5872.
13. Kojima, H., Muto, E., Higuchi, H. & Yanagida, T. (1997) *Biophys. J.* **73**, 2012–2022.
14. Svoboda, K., Schmidt, C. F., Schnapp, B. J. & Block, S. M. (1993) *Nature* **365**, 721–727.
15. Meyhofer, E. & Howard, J. (1995) *Proc. Natl. Acad. Sci. USA* **92**, 574–578.
16. Inoue, Y., Toyoshima, Y. Y., Iwane, A. H., Morimoto, S., Higuchi, H. & Yanagida, T. (1997) *Proc. Natl. Acad. Sci. USA* **94**, 7275–7280.
17. Case, R. B., Pierce, D. W., Hom-Booher, N., Hart, C. L. & Vale, R. D. (1997) *Cell* **90**, 959–966.
18. Smith, D. B. & Johnson, K. S. (1988) *Gene* **67**, 31–40.
19. Bradford, M. (1976) *Anal. Biochem.* **72**, 248–254.
20. Gallagher, S. R. (1995) in *Current Protocol in Protein Science*, eds. Coligan, J. E., Dunn, B. M., Speicher, D. W. & Wingfield, P. T. (Wiley, New York), Vol. 2, p. 10.3.1.
21. Kodama, T., Fukui, K. & Kometani, K. (1986) *J. Biochem. (Tokyo)* **99**, 1465–1472.
22. Harada, Y., Sakurada, K., Aoki, T., Thomas, D. D. & Yanagida, T. (1990) *J. Mol. Biol.* **216**, 49–68.
23. Nishiyama, M., Muto, E., Inoue, Y., Yanagida, T. & Higuchi, H. (2001) *Nat. Cell Biol.* **3**, 425–428.
24. Berliner, E., Mahtani, H. K., Karki, S., Chu, L. F., Cronan, J. E., Jr., & Gelles, J. (1994) *J. Biol. Chem.* **269**, 8610–8615.
25. Schatz, P. J. (1993) *Biotechnology* **11**, 1138–1143.
26. Svoboda, K. & Block, S. M. (1994) *Cell* **77**, 773–784.
27. Visscher, K. & Block, S. M. (1998) *Methods Enzymol.* **298**, 460–489.
28. Woehlke, G., Ruby, A. K., Hart, C. L., Ly, B., Hom-Booher, N. & Vale, R. D. (1997) *Cell* **90**, 207–216.
29. Alonso, M. C., van Damme, J., Vandekerckhove, J. & Cross, R. A. (1998) *EMBO J.* **17**, 945–951.
30. Rice, S., Lin, A. W., Safer, D., Hart, C. L., Naber, N., Carragher, B. O., Cain, S. M., Pechatnikova, E., Wilson-Kubalek, E. M., Whittaker, M., *et al.* (1999) *Nature* **402**, 778–784.
31. Hunt, A. J. & Howard, J. (1993) *Proc. Natl. Acad. Sci. USA* **90**, 11653–11657.
32. Kawaguchi, K. & Ishiwata, S. (2000) *Biochem. Biophys. Res. Commun.* **272**, 895–899.
33. Cross, R. A., Crevel, I., Carter, N. J., Alonso, M. C., Hirose, K. & Amos, L. A. (2000) *Philos. Trans. R. Soc. London B* **355**, 459–464.
34. Schief, W. R. & Howard, J. (2001) *Curr. Opin. Cell Biol.* **13**, 19–28.
35. Vale, R. D. & Milligan, R. A. (2000) *Science* **288**, 88–95.
36. Hirose, K., Lockhart, A., Cross, R. A. & Amos, L. A. (1996) *Proc. Natl. Acad. Sci. USA* **93**, 9539–9544.
37. Hua, W., Chung, J. & Gelles, J. (2002) *Science* **295**, 844–848.

Chemomechanical coupling of the forward and backward steps of single kinesin molecules

Masayoshi Nishiyama*†‡, Hideo Higuchi§¶†† and Toshio Yanagida*#**

*Single Molecule Processes Project, ICORP, JST, 2-4-14, Senba-Higashi, Mino, Osaka, 562-0035, Japan
†Department of Biophysical Engineering, Osaka University 1-3, Machikaneyama, Toyonaka, Osaka, 560-8531, Japan
§Department of Metallurgy, Graduate School of Engineering, Tohoku University, Sendai, 980-8579, Japan
¶Center of Interdisciplinary Research, Tohoku University, Sendai, 980-8579, Japan
#Department of Physiology and Biosignaling, Graduate School of Medicine, Osaka University, 2-2, Yamadaoka, Suita, Osaka, 565-0871, Japan
**Laboratories for Nanobiology, Graduate School of Frontier Biosciences Osaka University, A4, 2-2 Yamadaoka, Suita, Osaka, 565-0871, Japan
‡Current address: Department of Chemistry, Graduate School of Science, Kyoto University, Kyoto, 606-8502, Japan
††e-mail: higuchi@material.tohoku.ac.jp

Published online: 23 September 2002; doi 10.1038/ncb857

The molecular motor kinesin travels processively along a microtubule in a stepwise manner. Here we have studied the chemomechanical coupling of the hydrolysis of ATP to the mechanical work of kinesin by analysing the individual stepwise movements according to the directionality of the movements. Kinesin molecules move primarily in the forward direction and only occasionally in the backward direction. The hydrolysis of a single ATP molecule is coupled to either the forward or the backward movement. This bidirectional movement is well described by a model of Brownian motion assuming an asymmetric potential of activation energy. Thus, the stepwise movement along the microtubule is most probably due to Brownian motion that is biased towards the forward direction by chemical energy stored in ATP molecules.

Kinesin is a molecular motor that moves processively along a microtubule[1–5] with regular 8-nm steps[6–9]. Kinesin moves primarily in the forward direction (to the plus end of the microtubule) and occasionally in the backward direction (to its minus end), which has been commonly called a back step[10–13]. The maximum force against which single kinesin molecules work is 7 pN (refs 13–15).

To understand the mechanical properties of this mechanoenzyme, the relationship between force and sliding velocity has been investigated from averaged time courses of movement[10–16]. In previous studies, the back steps were included in the individual traces but were ignored in the analysis because they were considered to be rare events compared with the regular 8-nm steps in the forward direction.

The mechanism underlying these forward and backward movements remains unclear. Here we have characterized the stepping mechanism by correlating both the forward and the backward movements of single kinesin molecules to the hydrolysis of ATP.

Table 1 Rate constants of the branched kinetics

Force	Energy difference of the barriers*	Rate constants†				Velocity§	Run length¶
(pN)	(k_BT)	k_1 ($\mu M^{-1}\,s^{-1}$)	k_2 (s^{-1})	k_{3f} (s^{-1})	k_{3b} (s^{-1})	(nm s^{-1})	(nm)
0	5.4	3.4	140	770	3.5	930	3600
3.8	2.6	1.4	140	47	3.1	230	200
7.6	0	0.21	140	2.9	2.9	0	0

The parameters were calculated from the analysis of the dwell time for each force.
*Energy difference = $5.4k_BT - F \times 2.9$[nm].
†$k_1 = k_{on}/K_m$, $k_{on} = k_2(k_{3f} + k_{3b})/(k_2 + k_{3f} + k_{3b})$, $k_2 = 1/\tau_2$, $k_{3f} = R_0\exp(-Fd_1/k_BT)/(R_0+1)/\tau_3$, $k_{3b} = \exp(-Fd_b/k_BT)/(R_0 + 1)/\tau_3$, K_m = 36 μM (0 pN) and 27 μM (3.8 and 7.6 pN), τ_2 = 7.0 ms, τ_3 = 1.3 ms, R_0 = 221, d_1 = 3.0 nm, d_b = 0.1 nm.
§Velocity = 8[nm] × ε × k_{on} [s^{-1}], $\varepsilon = P_f - P_b = (k_{3f}/k_{3b} - 1)/(k_{3f}/k_{3b} + 1)$
¶Run length = 8[nm] × $(2P_f/P_b)$ × ε. The number of the stepwise movements until detachment occurred is described as $2P_f/P_b$, because the ratio of the detachment is roughly half the total number of movements in the backward direction. The ratio of detachment in total backward movement may be due to the experimental system.

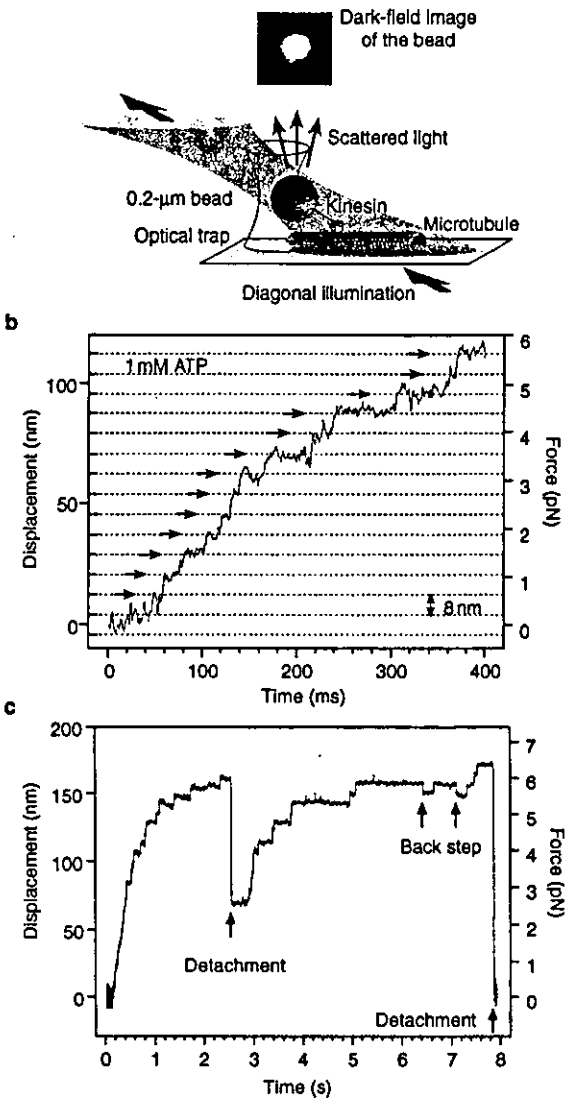

Figure 1 **Nanometry of single kinesin molecules. a**, The optical trapping nanometry system (not to scale). **b**, **c**, Time courses of the displacements of single kinesin molecules. The ATP concentration was 1 mM (**b**) and 10 μM (**c**). The displacement of kinesin was obtained from the bead displacement with the compliance of the experimental system (Methods). The force was calculated from the bead displacement and the trap stiffness (0.05 pN nm^{-1} in **b**; right axis).

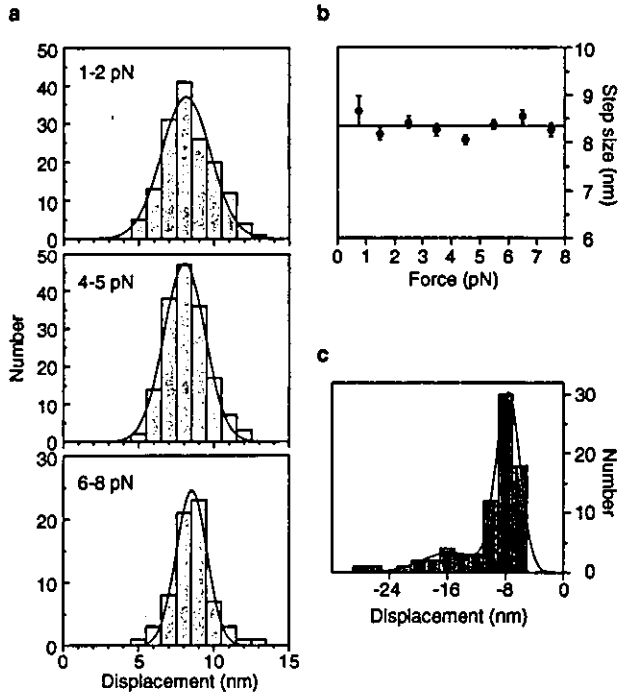

Figure 2 **Step size of the forward and backward movements. a**, Histograms of the step size at 10 μM ATP and forces of 1–2, 4–5 and 6–8 pN. Lines are the best fits of the data to a gaussian curve; the peak position and width are 8.2 and 1.6 nm (1–2 pN), 8.1 and 1.1 nm (4–5 pN), and 8.4 and 0.9 nm (6–8 pN), respectively. **b**, Step size as a function of load. The step sizes (mean ± s.e.m.) were obtained from the peak position in **a** at each load (ATP concentration 10 μM, n = 13–177, total = 937). The average step size at each load is 8.3 nm (line). **c**, Histogram for the step sizes of the back steps. Displacement data (<30 nm) at ATP concentrations of 1 mM and 10 μM are included. The line is the sum of two gaussian peaks fitted to the data; the positions and widths of each peak are −7.7 and 1.6 nm, and −15.5 and 4.1 nm (twice the displacement at the main peak), respectively. The 16-nm step cannot be resolved into two 8-nm steps even at the submillisecond temporal resolution. It is likely that the 16-nm steps are induced in a single cycle of ATP hydrolysis, indicating that the back step may be due to the rebinding of kinesin to other sites of the microtubule after detachment.

Results

Stepwise movements of single kinesin molecules. Single kinesin molecules were attached to a bead captured by an optical trap and brought into contact with a microtubule attached to a glass surface (Fig. 1a). The bead was illuminated diagonally by a focused red laser and its dark field image was projected onto a quadrant photodiode. The displacement of the bead was determined by measuring the differential output of the quadrant photodiode with nanometer accuracy[17].

The time course of kinesin movement showed a distinctive stepwise pattern with regular 8-nm steps at forces greater than 0.5 pN; this regular step size is clearly indicated by the lines drawn at 8-nm intervals in Fig. 1b. Kinesin moved primarily in the forward direction but occasionally in the backward direction (Fig. 1c, arrows). We characterized these stepwise movements by analysing the force, step size and dwell time between the stepwise movements.

The step size was determined directly from the distinctive pattern of movements in the time courses for kinesin (see Methods). For the forward steps, the step size was 8 nm and was independent of the load (Fig. 2a, b) and ATP concentration (8.0 and 8.3 nm at ATP concentrations of 1 mM and 10 μM, respectively). For the back steps, the step size was either 8 nm or 16 nm (Fig. 2c) and was independent of the load and ATP concentration (data not shown).

We also tested whether other short steps existed in the dwell time between the 8-nm steps[7,16,18,19]. Typical traces of the region between the adjacent 8-nm steps on an expanded timescale showed no evidence of short steps (Fig. 3a). To measure changes in displacement with greater accuracy, we averaged the traces after synchronizing the rising phases of the 8-nm steps at the start and end of the dwell time[20]. The averaged traces did not show any significant displacements (>1 nm) in the dwell time at temporal resolution of 1 ms (Fig. 3b). Similar results were also obtained from analysis of the back steps (data not shown). Thus, kinesin moves only in 8-nm steps in the forward direction and in 8-nm and 16-nm steps in the backward direction, but not in steps shorter than 8 nm.

Directionality of the step. Kinesin moved primarily in the forward direction at low loads. The occurrence of back steps (step size <30 nm) and detachments (>30 nm) increased with the load

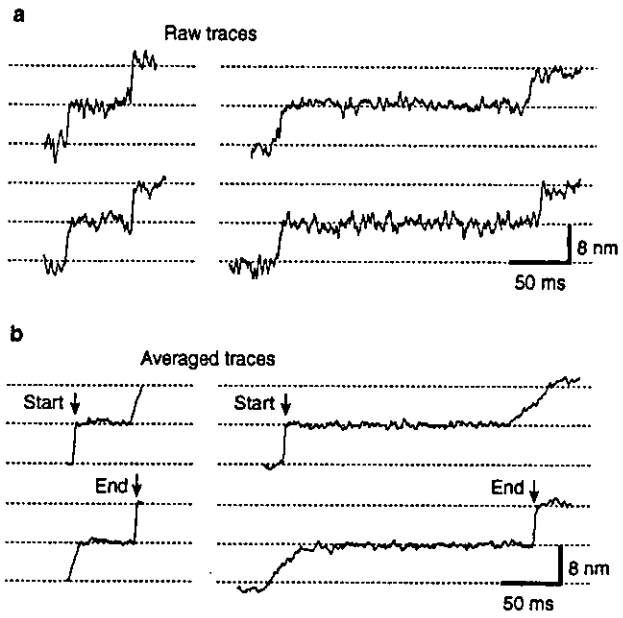

Figure 3 **Displacements of kinesin in the dwell time. a**, Raw traces of the stepwise displacements recorded with a bandwidth of 500 Hz. **b**, Traces averaged at the start and end step of the dwell time. The raw stepwise movements shown in **a** were collected from the time courses at forces of 1–7 pN (left, dwell time 50 ± 5 ms, n = 37; right, dwell time 200 ± 20 ms, n = 15). The top traces were obtained by averaging the individual time courses after synchronizing the 4-nm points of the 8-nm steps ('start' step, arrows). The accuracy of the averaging procedures was about 1 ms, which was verified by the rise time of the individual averaged traces (corresponding to the displacement from 1 nm to 7 nm). The bottom traces were obtained by averaging the traces at the 4-nm point of the 'end' step. The ATP concentration was 10 μM (**a** and **b**).

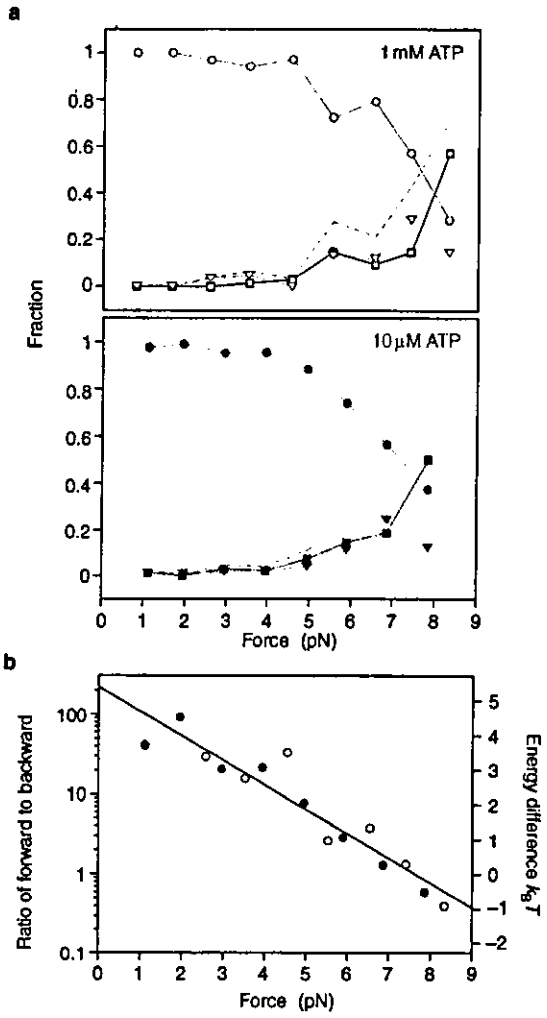

Figure 4 **Step directionality. a**, Fraction of 8-nm steps (circles), back steps (triangles) and detachments (squares) as a function of the force. Fractions were obtained from the number of 8-nm steps, back steps and detachments at each force in the presence of 1 mM (n = 5–69, total = 380) and 10 μM ATP (n = 8–186, total = 990). **b**, Ratio of the forward to backward movements. Data were obtained at 1 mM ATP (open circles) and 10 μM (filled circles). Data are not plotted for points where backward movements were not observed. The plots at 1 mM and 10 μM ATP were fitted to equation (1), with R_0 = 221 and d = 2.9 nm. The energy difference between the backward and forward direction barriers is shown on the right.

(Fig. 1c). We analysed the direction of movement by counting the number of 8-nm steps, back steps and detachments as a function of the load at 1-pN intervals from 0.5 pN to 8.5 pN at ATP concentrations of 1 mM and 10 μM (Fig. 4a). At loads lower than 4 pN the fraction of 8-nm steps was almost equal to 1, indicating that almost all steps were made in the forward direction. As the load increased, the fraction of the 8-nm steps gradually decreased.

Correspondingly, the occurrence of back steps and detachments increased with an increase in load. The sums of them are plotted as the 'backward movements' (dotted lines) with respect to the 'forward movements' (8-nm steps) in Fig. 4a. The fraction of backward movements increased exponentially with load and intersected with that of the forward movements at 7–8 pN.

We characterized the load dependence of the stepping direction by calculating the ratio of the forward to the backward movements at each load. The ratio decreased exponentially with load, and the plots of ratio against load in the presence of 1 mM and 10 μM ATP could almost be superimposed (Fig. 4b). These results show that the fraction of forward and backward movements is dependent on load but not on the concentration of ATP. Thus, the load modifies the stepping motion, resulting in unidirectional movements.

Dwell time. To relate the 8-nm steps, back steps and detachments to the kinetic pathway, we analysed the dwell time between the stepwise movements. The dwell time was directly measured from the movement time courses and averaged at each load and ATP concentration for the different types of stepwise movement (see Methods). Figure 5a shows the average dwell times before an 8-nm step at saturating (1 mM) and limiting (10 μM) concentrations of ATP. The dwell time increased with load and decreased with concentration of ATP. The relationship between force and dwell time at an ATP concentration of 1 mM, plotted on the log scale, deviated from a straight line (data not shown). This means that the relationship between force and dwell time cannot be described by a simple exponential curve. The dwell time at saturating ATP concentrations has been shown to comprise load-dependent and load-independent transitions[21,22]. Taking into consideration the fact that the ATP binding reaction is limiting at low ATP concentrations, there are at least three transitions in a single dwell time.

Figure 5b summarizes the dwell time before the occurrence of back steps and detachments. Each plot is the average dwell time at each ATP concentration, obtained using the method used for the 8-nm steps. Notably, the dwell time of the back steps and detachments was altered by the load and the ATP concentration. The backward movements did not occur easily under high loads and limiting ATP concentrations, similar to that found for the forward

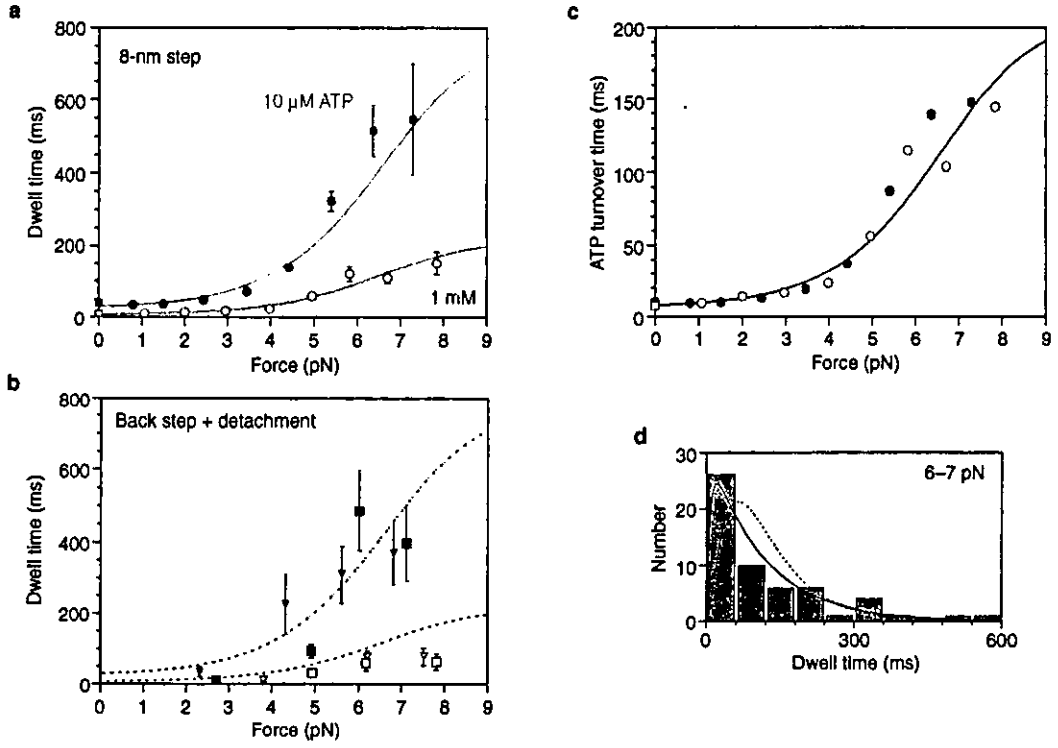

Figure 5 **Dwell time between the adjacent stepwise movements. a**, Dwell time before the 8-nm step as a function of force. Each point represents the average dwell time at ATP concentrations of 1 mM (open circles, n = 21–64, total = 327) and 10 μM (filled circles, n = 13–177, total 889). The curves were obtained from equations (3) and (6). **b**, Dwell time before the back step and detachment. Each plot is the average value of the dwell time at 1 mM ATP (back step (open triangles), n = 8–9, total = 25; detachment (open squares), n = 9–10, total = 28) and 10 μM ATP (back step (filled triangles), n = 6–18, total = 46; detachment (filled squares), n = 6–23, total = 63). The dotted curves represent the unbroken lines in **a** and are included for comparison. **c**, ATP turnover time was calculated from the dwell time in **a** with equation (6) and K_m = 27 μM. Plots in the presence of 1 mM (open circles) and 10 μM (filled circles) ATP have been fitted by equation (3) with τ_2 = 7.0 ms, τ_3 = 1.3 ms and d_f = 3.0 nm. **d**, Histogram of the dwell time before an 8-nm step at 6–7 pN. The ATP concentration was 1 mM. The unbroken line is the fitting curve obtained from simulating the three-step reaction model shown in Fig. 6a with Lab VIEW v.5.1 (National Instruments)[13]. Three rate constants were calculated from the equations and parameters (Table 1). The broken line was obtained by simulating the futile hydrolysis model, in which a single dwell time corresponds to two cycles of the same three-step reactions (six-step reactions in total).

movements (Fig. 5a). In fact, the dwell time of the back steps and detachments could be essentially described by the curve fit used for the 8-nm steps (Fig. 5b, dotted lines, and see below). Thus, the forward and backward movements may be coupled to the same kinetic pathway for the hydrolysis of ATP molecules.

According to Michaelis–Menten kinetics, a single dwell time consists of the ATP binding and hydrolysis reactions. The former is characterized by the Michaelis constant, K_m, which in this case describes the affinity of kinesin for ATP. We calculated the K_m at each load from the ratio of the dwell time at 10 μM ATP to that at 1 mM ATP using equation (7) in Methods. The ratio was 3.8, 3.2 and 3.6 at 1, 3 and 5 pN, respectively (average ratio 3.7), and was therefore independent of the force. Thus, the K_m was 27 μM irrespective of the load, which enabled us to calculate the ATP turnover time. Figure 5c plots the relationship between force and ATP turnover time at ATP concentrations of 1 mM and 10 μM; the two plots can be essentially described by the same curve (see below). Our results indicate that the ATP binding reaction for kinesin is independent of the load, which differs from the results of previous studies[15,16]. This discrepancy might be due to the different approaches used for calculating the ATPase reaction: whereas we used the individual dwell time for the 8-nm steps, other studies used values obtained from averaged time traces[15,16].

Analysis of the bidirectional steps. We incorporated the forward and backward movements into a three-state model with some modifications[18]. The three states of K, K.T and K.D considered in the analysis correspond to kinesin with no bound nucleotide, with bound ATP and with bound ADP (or ADP.Pi), respectively (Fig. 6a). The forward (f) and backward (b) movements occur in parallel, such that the kinetic pathway branches at the K.D state. The rate constant from K.D to K is given as the sum of k_{3f} and k_{3b}. The ratio of the forward to backward movements is equal to k_{3f}/k_{3b}. According to Arrhenius/Eyring kinetics, the rate constant is related to the activation energy of the barrier potential. We therefore used an asymmetric potential to analyse the bidirectional stepwise movements.

The activation energy of the forward and backward directions can be described by $E_f + Fd_f$ and $E_b + Fd_b$, respectively, where E_f and E_b are the heights of the barrier maximum at zero load, and d_f and d_b are the characteristic distances against the load F (Fig. 6b). If the Boltzmann energy distribution is assumed, then the rates in the forward and backward direction will be proportional to $\exp[-(E_f + Fd_f)/k_BT]$ and $\exp[-(E_b + Fd_b)/k_BT]$, respectively[21], where k_B is the Boltzmann constant and T is the experimental temperature (298 K). The number of forward movements relative to the backward is equal to k_{3f}/k_{3b} under kinetic control and is given by:

$$k_{3f}/k_{3b} = R_0\exp(-Fd/k_BT) \quad (1)$$

$$d = d_f - d_b \quad (2)$$

where $R_0 = \exp[(E_b - E_f)/k_BT]$ is the ratio of the rate constants at no

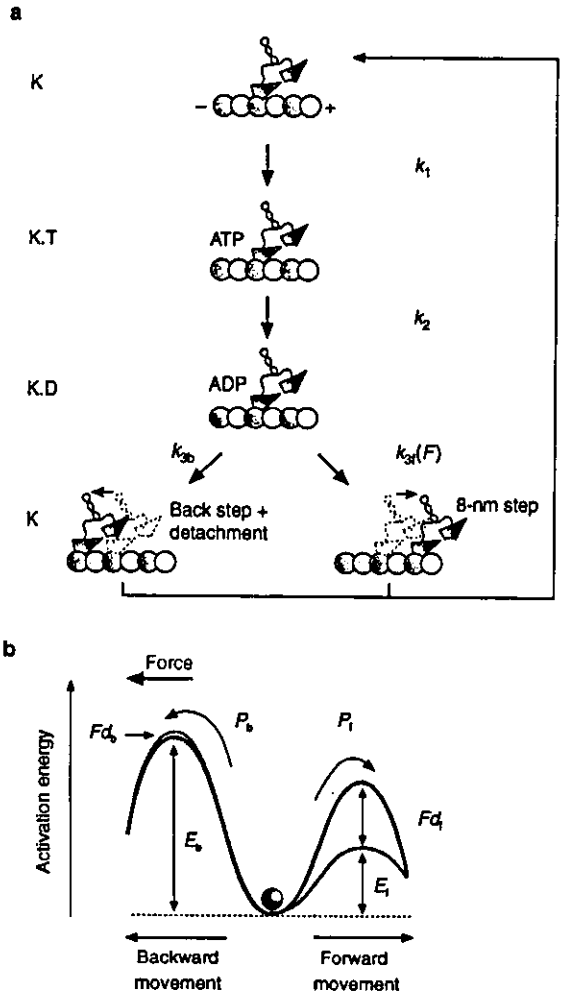

Figure 6 **Stepping kinetics of the bidirectional movements. a**, Branched kinetic pathway. Kinesin attached to the microtubule with one motor domain (state K). The ATP molecule binds to the head (state K.T) and is hydrolysed (state K.D). After kinesin moves either to the forward or backward direction, the ADP molecules are released (state K). **b**, Asymmetric potential of the activation energy (see text).

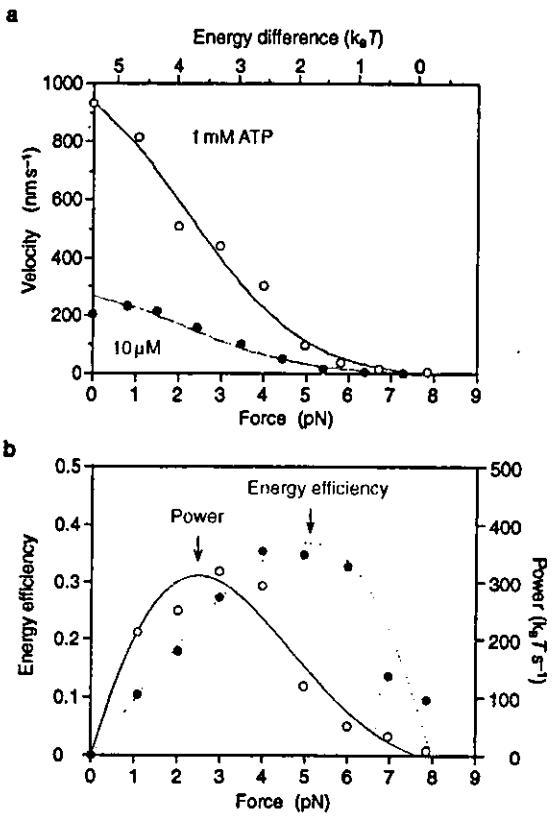

Figure 7 **Mechanics and energetics.** The stepping efficiency is $\varepsilon(F) = P_f - P_b$, where P_f and P_b are the probabilities of the forward and backward movements ($P_f + P_b = 1$), respectively, and F is the force. Each ATP hydrolysis reaction is assumed to result in a stepwise movement. The step size of the backward movement has been standardized to 8 nm. **a**, Force–velocity relationships. Velocities in the presence of 1 mM (open circles) and 10 μM (filled circles) ATP were calculated as $L\varepsilon/\tau$, where L is the step size of 8 nm and τ is the average dwell time. When the force–velocity relation is normalized to zero load levels, the velocity is no longer dependent on the ATP concentration. The energy difference between the backward and forward direction barriers is shown on the top axis. **b**, Energy efficiency and power. Work is defined as $W = LF\varepsilon$. The energy efficiency, E, and power, P, at an ATP concentration of 1 mM were obtained from $E = W/(20k_BT)$ (filled circles and dotted line; left axis) and $P = W/\tau$ (open circles and unbroken line; right axis).

load and d is the difference of the characteristic distances. The plots in Fig. 4b were fitted by equation (1), with $R_0 = 221$ and $d = 2.9$ nm. The energy difference between the backward and forward direction barrier maximums was 5.4 k_BT at zero load, and the difference decreased linearly with load. When the load reached 7.6 pN, the barrier height of the forward direction was equal to that of the backward direction, and the directionality of the motion disappeared. Thus, the stall force could be determined as the force at which the probabilities of the forward and backward movements were equal.

According to our branched three-state model, the ATP turnover time, τ_{cat}, is composed of the inverse of k_2 and the inverse of $k_{3f} + k_{3b}$. Thus, τ_{cat} is given by:

$$\tau_{cat} = \tau_2 + \tau_3 \cdot \left\{ \left(\frac{R_0}{R_0 + 1} \right) e^{-Fd_f/k_BT} + \left(\frac{1}{R_0 + 1} \right) e^{-F(d_f - d)/k_BT} \right\}^{-1} \quad (3)$$

where τ_2 is $1/k_2$ and is independent of the load, and τ_3 is $1/(k_{3f} + k_{3b})$ in the absence of a load[21,22]. The ATP turnover time at ATP concentrations of 1 mM and 10 μM (Fig. 5c) could be well fitted by equation (3), with $\tau_2 = 7.0$ ms, $\tau_3 = 1.3$ ms and $d_f = 3.0$ nm. In addition, d_b was calculated to be 0.1 nm by equation (2). The small value of d_b indicates that the backward barrier height is not greatly altered by the effect of a load. Table 1 shows the summary of the rate constants at 0, 3.8 and 7.6 pN (the stall force), which is consistent with previous studies using either a single-molecule assay[8,13] or steady-state kinetics[23,24]. Thus, load dependence of the dwell time can be mainly ascribed to the rate constant of k_{3f}.

In the above discussion, we assumed that each cycle of the ATP hydrolysis reaction is coupled to a stepwise movement. This assumption has been confirmed at low loads[9,15,25] but not at high loads. We therefore characterized the chemomechanical coupling at high loads by studying the possibility of 'futile hydrolysis'[15,16] — that is, the possibility that ATP is hydrolysed but kinesin fails to generate the movement. The histogram of the dwell time before an 8-nm step at 6–7 pN shows a monotonic decrease (Fig. 5d), consistent with our model in which the kinetic pathway has one rate limiting reaction at high loads and saturating ATP concentrations. If the futile hydrolysis reactions occur frequently at high loads, then the result would be a large shift in the position of peaks or the

occurrence of the additional peaks. Such changes were not apparent in Fig. 5d.

We next determined the number of ATP molecules consumed at each stepwise movement by trying to fit the dwell time histogram with curves corresponding to simple hypotheses[25,26]. The histogram could be fitted to the curve by assuming that one ATP molecule is always consumed per stepwise movement (unbroken line, reduced $\chi^2 = 1.1$), but not by assuming that two ATP molecules were consumed per stepwise movement (broken line, reduced $\chi^2 = 5.6$). Thus, the latter hypothesis was rejected at a significance of less than 1% using the χ^2-test. Similar results were obtained from the dwell time histogram at other force levels. Therefore, futile hydrolysis reactions do not occur frequently even at high loads, indicating that the hydrolysis reaction of ATP molecules for kinesin most probably results in a stepwise movement.

Mechanics and energetics of the stepwise movements. We characterized the mechanical and energetic aspects of the bidirectional movements of kinesin by calculating the velocity, run length, energy efficiency per ATP turnover and power. Our calculations using data from individual steps enabled us to compare our results with previous values obtained from averaged traces.

Figure 7a shows the force–velocity curves of the stepwise movements; these did not show linear[10–14] or upper concave[15,16] relationships, as found in previous studies, but were more similar to the inverse proportion[27]. This discrepancy is most probably due to the different methods used for calculating the velocity, that is, individual stepwise movements (used here) versus those obtained from averaged traces[10–16]. We estimated the run length of kinesin along a microtubule from the stepping efficiency (Table 1). The run length at zero load was about 3 μm, which is reasonably consistent with previous values[2–4,14,28]. When a load was applied to kinesin, the run length decreased exponentially with the increment of the load[16] and reached zero at 7.6 pN (Table 1). We characterized the energetic aspects of the bidirectional movement by the energy efficiency and power, which we calculated from the work taking into account the stepping efficiency (Fig. 7b). The energy efficiency and power showed peaks at moderate loads, but these peaks had different positions. Notably, similar results have been reported for studies using muscle fibres[27].

Discussion

We have analysed the individual stepwise movements — that is, the 8-nm steps, back steps (<30 nm) and detachments (>30 nm) — of kinesin travelling along microtubules. It seems that the hydrolysis of single ATP molecules can be coupled to either the forward or the backward movement. This indicates that the chemomechanical coupling is not deterministic. Thus, kinesin may be a loosely coupled motor because the ATP hydrolysis reaction does not necessarily couple to the forward movement. How the forward and backward movements are created through hydrolysis of ATP is outlined below and in Fig. 6a.

In the absence of ATP, kinesin molecules attach to a microtubule through one head (rigor), leaving the other one free (refs 29, 30; state 'K'). ATP molecules bind to the head that is linked to the microtubule according to Michaelis–Menten kinetics (refs 2, 24; state 'K.T'). We obtained a Michaelis constant of 27 μM, and this value is independent of the load[11]. Because the stepwise movements take place through a load-dependent transition (Fig. 4), kinesin is not able to move in the forward direction in the K.T state. The nucleotide hydrolysis process from ATP to ADP (state 'K.D') causes a structural change of the kinesin head[31,32], such that the binding between kinesin and the microtubule is changed to a highly mobile state[33,34].

The unidirectional movement of kinesin has never been reported in the presence of ADP, but no ATP; thus, the free energy released from ATP hydrolysis is essential for creating the 8-nm step. This energy may be stored in the ATP molecules[16,35], as demonstrated by a load-dependent asymmetric potential (Fig. 6b). Kinesin in the energy-charged K.D state is able to make an 8-nm step, although there is also the risk of a back step or detachment. After the kinesin molecule moves to the next binding site, the ADP molecule is released and the head returns to the immobile state at the new binding site (state 'K'). This rapid dissociation might be involved in inhibiting any additional movements, such that kinesin makes only a single stepwise movement at each hydrolysis of ATP.

The load dependence of the stepwise movements is characterized primarily by the large characteristic distance, $d_f = 3.0$ nm, which indicates the existence of substeps[16,18]. In our experiments, however, analysis in the millisecond time range showed no evidence of steps shorter than 8 nm (Figs 2 and 3). Thus, the most likely explanation is that the substep coincides with the rising phase of the 8-nm step. This has already been proved by measuring the nanometre displacements of kinesin with microsecond accuracy, showing that the 8-nm step is composed of sequential 4-nm substeps[17]. These rapid two-step reactions can be explained by a 'hand-over-hand' process, in which the two heads of kinesin work in a coordinated manner[18,36]. A structural change in the motor domain initiates the partner head to attach to the next binding site, which is 8 nm from the initial binding site[28,31]. The rear head then detaches from the initial binding site. In this mechanism, the role of each head would alternate at each ATPase cycle.

But it has been reported that single one-headed kinesin molecules can move processively along the microtubule[37,38]. This indicates that the two-headed structure is not required for motility, because a stepwise movement can be achieved by single head. Thus, the role of the partner head might be to stabilize the kinesin–microtubule complex, similar to the K-loop of the KIF1 motor[38,39] or to biotin-dependent transcarboxylase (BDTC) in single-headed kinesin[37], and assist in movements towards the plus end of the microtubule[31]. To move for a considerable distance, such as the length of the motor domain (7 nm), the head that is attached to the microtubule might step along the 4-nm repeat of tubulin monomers[40,41] in a way that resembles hopping on one leg.

The stochastic behaviour of the forward and backward movements can be explained simply by a model of biased Brownian motion. Because Brownian motion is random, it must be biased in the forward direction to produce the unidirectional movement observed. In this study the forward and backward movements can be explained by the Brownian motion of a mass particle on a one-dimensional asymmetric potential of activation energy. According to the Arrhenius/Eyring kinetics, the asymmetry of the potential is ascribed to the different height of the barrier maximum; the energy difference is 5.4 k_BT (where $T = 298$ K) at zero load, which is about a quarter of the free energy of the ATP hydrolysis (~20 k_BT).

Alternatively, another idea for the biased Brownian motion has been proposed on the basis of the thermal ratchet model[42–44]. In this model, a simple motor consists of a ratchet and a pawl isolated at different temperatures that produces work and unidirectional motion. Two temperatures, T_f and T_b, control the probabilities of the forward and backward steps of motor molecules, respectively; in general, $T_f > T_b = T$ (the experimental temperature). In the thermal ratchet model, the probability of the forward movement but not the backward movement is dependent on the load. This is consistent with our results. Here, we calculated T_f from the ratio of the forward to the backward movement (Fig. 4b). We characterized an asymmetric potential assuming that the barrier height is E ($E = E_f = E_b$, regardless of the load) and the distance from the bottom to the forward barrier maximum is equal to the step size, thus, $d_f = 8$ and $d_b = 0$ nm. The experimental data were fitted by $T_f = 2.8\ T$, leading to $T_f = 834$ K at the experimental temperature $T = 298$ K. The energy barrier in the potential was 8.4 k_BT, which is roughly half of the free energy of the ATP hydrolysis.

We used these procedures to estimate the T_f of the other processive motor molecules — 22S dynein of *Tetrahymena* cilia[45], the inner-arm dynein c of *Chlamydomonas* flagella[46] and myosin V

(ref. 22) — from the ratio of the step size to the characteristic distance. Notably, the T_f of these motors is about $3T$ (~900 K), which is almost the same as that of kinesin. Thus, the ATP-driven processive motors, kinesin, dynein and myosin, would seem to be programmed to work with the same chemomechanical energy transduction mechanism.

We conclude that the forward and backward movements of kinesin are created by a similar chemomechanical energy transduction mechanism. The stepwise movement is essentially Brownian motion that is biased in the forward direction. The biased Brownian motion is caused by the interaction between kinesin and the microtubule, which is dynamically changed by the free energy derived from the hydrolysis of ATP. □

Methods

Single-molecule assays

We obtained kinesin and tubulin from bovine brains and purified them as described[8,13]. Tubulin was labelled with tetramethylrhodamine succinimidyl ester and then polymerized into microtubules. We carried out single-molecule assays by using the improved optical trapping nanometry system[17] with some modifications.

Kinesin was mixed with bead solution at a molar ratio of kinesin to beads of 0.5, so that the kinesin-coated beads moved onto the microtubule with a probability of 0.31. Taking the geometry of the kinesin on the bead into account[10,13], the probability that a single kinesin molecule would interacting with a microtubule was 0.95. We discarded the results from beads with a maximum force of more than 9 pN, because it was thought that on these beads more than two kinesin molecules were binding to a microtubule. All the procedures were done at 25 ± 1 °C.

Nanometry of the stepwise movements

We recorded the bead displacements at a sampling rate of 20 kHz with a bandwidth of 10 kHz. The force of kinesin was calculated from the bead displacement multiplied by the trap stiffness (0.03–0.06 pN nm^{-1}), which was determined from the variance of the thermal fluctuations of a trapped bead with the equipartition theorem of energy[17]. Kinesin displacements were calculated from the bead displacements with an attenuation factor at each force[13]. The average values of the attenuation factor obtained from the thermal fluctuation of the bead between the adjacent stepwise movements[17] were 1.35, 1.10 and 1.06 at 1, 4 and 7 pN, respectively; the attenuation factor was inversely proportional to the load[8].

The stepwise movements of kinesin were clearly observed after the time record was filtered with a bandwidth of 500 Hz; the noise between the stepwise movements was about 1 nm (the standard deviation over the interval of 10 ms was 1.63, 0.88 and 0.73 nm at 1, 4 and 7 pN, respectively). The step size for the forward and backward movements was obtained directly from the individual stepwise movements and determined as the difference between the average kinesin positions over a 5-ms interval before and after the step.

The dwell time between 8-nm steps at near zero loads was estimated to be about 8 ms on average. This value was obtained by dividing the sliding velocity (960 nm s^{-1}) by the step size (8 nm). Therefore, submillisecond resolution is required for detecting the individual stepwise movements. The temporal resolution for the experimental system was checked from the response time of the force generation of kinesin-coated bead[17]. This temporal resolution was essentially retained after passing through the filter. This was confirmed by the absence of any large steps >16 nm (ref. 15) in the raw traces (Figs 1 and 3) and histograms of the step size (Fig. 2a). Thus, our experimental system was equipped with a spatial and temporal resolution that was sufficient to detect all stepwise movements in the time courses studied.

Dwell time

The dwell times between the adjacent stepwise movements were classified into three groups: an 8 nm step at the end phase of the dwell time, a back step (<30 nm), and a detachment (>30 nm). The dwell time was measured as the time from the midpoint of a stepwise movement to that of the next in the bead traces passed through a low-pass filter with a bandwidth of 500 Hz. The dwell time for the 8-nm step had a distribution with a peak at high resolution. Thus, the average dwell time was obtained by integrating the histogram of the dwell time and fitting it to the two-step reaction equation by least squares[8].

The average dwell time at 0 pN was estimated from the step size (8 nm) divided by the sliding velocity without the optical trap. The sliding velocity of kinesin was measured from the image analysis of bead image[17] at ATP concentrations between 1 and 1,000 μM. At very low ATP concentrations, an ATP regenerating system (1 mM phosphoenolpyrubic acid and 10 unit/ml phosphoenolpyruvate carboxykinase, final concentrations) was added to the solution. The relationship between the velocity and ATP concentration was fitted to the Michaelis–Menten kinetics equation with K_m = 36 ± 3 μM and V_{max} = 960 ± 50 nm s^{-1}, consistent with previous studies[8,11].

ATP turnover time

According to novel Michaelis–Menten kinetics, the sliding velocity of the motor molecules, V, is described as

$$V = \frac{V_{max} \cdot [ATP]}{[ATP] + K_m} \quad (4)$$

where V_{max} is the sliding velocity at saturating concentrations of ATP and K_m is the Michaelis constant[18,11]. In consideration of the stepwise movement of kinesin molecules, the microscopic velocity was defined as the step size (8 nm) divided by the dwell time, τ, between adjacent steps. Thus, the equation (4) can be described as

$$\frac{8}{\tau} = \frac{8}{\tau_{cat}}\left(\frac{[ATP]}{[ATP] + K_m}\right) \quad (5)$$

where τ_{cat} is the ATP turnover time and this corresponds to the dwell time at saturating concentrations of ATP. The ATP turnover time was calculated from

$$\tau_{cat} = \tau / \left(1 + \frac{K_m}{[ATP_{limit}]}\right) \quad (6)$$

The dwell times in the presence of saturating (>>Km) and limiting (<Km) ATP are represented for τ_{cat} and τ_{limit}, respectively. The ratio of τ_{limit} to τ_{cat} was calculated as follows

$$\tau_{limit} / \tau_{cat} = \left(1 + \frac{K_m}{[ATP_{limit}]}\right) \quad (7)$$

If the ratio of the dwell times is not changed by the load, then Km is independent of the load.

RECEIVED 22 FEBRUARY 2002; REVISED 8 JULY 2002; ACCEPTED 27 AUGUST 2002; PUBLISHED 23 SEPTEMBER 2002.

1. Vale, R. D., Reese, T. S. & Sheetz, M. P. Identification of a novel force-generating protein, kinesin, involved in microtubule-based motility. *Cell* 42, 39–50 (1985).
2. Howard, J., Hudspeth, A. J. & Vale, R. D. Movement of microtubules by single kinesin molecules. *Nature* 342, 154–158 (1989).
3. Block, S. M., Goldstein, L. S. B. & Schnapp, B. J. Bead movement by single kinesin molecules studied with optical tweezers. *Nature* 348, 348–352 (1990).
4. Hackney, D. D. Highly processive microtubule-stimulated ATP hydrolysis by dimeric kinesin head domains. *Nature* 377, 448–450 (1995).
5. Vale, R. D. *et al.* Direct observation of single kinesin molecules moving along microtubules. *Nature* 380, 451–453 (1996).
6. Svoboda, K., Schmidt, C. F., Schnapp, B. J. & Block, S. M. Direct observation of kinesin stepping by optical trapping interferometry. *Nature* 365, 721–727 (1993).
7. Coppin, C. M., Finer, J. T., Spudich, J. A. & Vale, R. D. Detection of sub-8-nm movements of kinesin by high-resolution optical-trap microscopy. *Proc. Natl Acad. Sci. USA* 93, 1913–1917 (1996).
8. Higuchi, H., Muto, E., Inoue, Y. & Yanagida, T. Kinetics of force generation by single kinesin molecules activated by laser photolysis of caged ATP. *Proc. Natl Acad. Sci. USA* 94, 4395–4400 (1997).
9. Hua, W., Young, E. C., Fleming, M. L. & Gelles, J. Coupling of kinesin steps to ATP hydrolysis. *Nature* 388, 390–393 (1997).
10. Svoboda, K. & Block, S. M. Force and velocity measured for single kinesin molecules. *Cell* 77, 773–784 (1994).
11. Meyhöfer, E. & Howard, J. The force generated by a single kinesin molecule against an elastic load. *Proc. Natl Acad. Sci. USA* 92, 574–578 (1995).
12. Coppin, C. M., Pierce, D. W., Hsu, L. & Vale, R. D. The load dependence of kinesin's mechanical cycle. *Proc. Natl Acad. Sci. USA* 94, 8539–8544 (1997).
13. Kojima, H., Muto, E., Higuchi, H. & Yanagida, T. Mechanics of single kinesin molecules measured by optical trapping nanometry. *Biophys. J.* 73, 2012–2022 (1997).
14. Kawaguchi, K. & Ishiwata, S. Temperature dependence of force, velocity, and processivity of single kinesin molecules. *Biochem. Biophys. Res. Commun.* 272, 895–899 (2000).
15. Visscher, K., Schnitzer, M. J. & Block, S. M. Single kinesin molecules studied with a molecular force clamp. *Nature* 400, 184–189 (1999).
16. Schnitzer, M. J., Visscher, K. & Block, S. M. Force production by single kinesin motors. *Nature Cell Biol.* 2, 718–723 (2000).
17. Nishiyama, M., Muto, E., Inoue, Y., Yanagida, T. & Higuchi, H. Substeps within the 8-nm step of the ATPase cycle of single kinesin molecules. *Nature Cell Biol.* 3, 425–428 (2001).
18. Howard, J. *Mechanics of Motor Proteins and the Cytoskeleton* (Sinauer Associates, Sunderland, MA, 2001).
19. Fisher, M. E. & Kolomeisky, A. B. Simple mechanochemistry describes the dynamics of kinesin molecules. *Proc. Natl Acad. Sci. USA* 98, 7748–7753 (2001).
20. Veigel, C. *et al.* The motor protein myosin-I produces its working stroke in two steps. *Nature* 398, 530–533 (1999).
21. Wang, M. D. *et al.* Force and velocity measured for single molecules of RNA polymerase. *Science* 282, 902–907 (1998).
22. Mehta, A. D. *et al.* Myosin-V is a processive actin-based motor. *Nature* 400, 590–593 (1999).
23. Gilbert, S. P., Webb, M. R., Brune, M. & Johnson, K. A. Pathway of processive ATP hydrolysis by kinesin. *Nature* 373, 671–676 (1995).
24. Ma, Y. Z. & Taylor, E. W. Mechanism of microtubule kinesin ATPase. *Biochemistry* 34, 13242–13251 (1995).
25. Schnitzer, M. J. & Block, S. M. Kinesin hydrolyses one ATP per 8-nm step. *Nature* 388, 386–390 (1997).
26. Rief, M. *et al.* Myosin-V stepping kinetics: a molecular model for processivity. *Proc. Natl Acad. Sci. USA* 97, 9482–9486 (2000).

27. Woledge, R. C., Curtin, N. A. & Homsher, E. *Energetic Aspects of Muscle Contraction* 167–275 (Academic, London, 1985).
28. Tomishige, M. & Vale, R. D. Controlling kinesin by reversible disulfide cross-linking: identifying the motility-producing conformational change. *J. Cell Biol.* 151, 1081–1092 (2000).
29. Hirose, K., Lockhart, A., Cross, R. A. & Amos, L. A. Three-dimensional cryoelectron microscopy of dimeric kinesin and ncd motor domains on microtubules. *Proc. Natl Acad. Sci. USA* 93, 9539–9544 (1996).
30. Kawaguchi, K. & Ishiwata, S. Nucleotide-dependent single- to double-headed binding of kinesin. *Science* 291, 667–669 (2001).
31. Rice, S. *et al.* A structural change in the kinesin motor protein that drives motility. *Nature* 402, 778–784 (1999).
32. Kikkawa, M. *et al.* Switch-based mechanism of kinesin motors. *Nature* 411, 439–445 (2001).
33. Romberg, L. & Vale, R. D. Chemomechanical cycle of kinesin differs from that of myosin. *Nature* 361, 168–170 (1993).
34. Sosa, H., Peterman, E. J. G., Moerner, W. E. & Goldstein, L. S. B. ADP-induced rocking of the kinesin motor domain revealed by single-molecule fluorescence polarization microscopy. *Nature. Struct. Biol.* 8, 540–544 (2001).
35. Kitamura, K., Tokunaga, M., Iwane, A. H. & Yanagida, T. A single myosin head moves along an actin filament with regular steps of 5.3 nanometres. *Nature* 397, 129–134 (1999).
36. Vale, R. D. & Milligan, R. A. The way things move: looking under the hood of molecular motor proteins. *Science* 288, 88–95 (2000).
37. Inoue, Y., Iwane, A. H., Miyai, T., Muto, E. & Yanagida, T. Motility of single one-headed kinesin molecules along microtubules. *Biophys. J.* 81, 2838–2850 (2001).
38. Okada, Y. & Hirokawa, N. Mechanism of the single-headed processivity: diffusional anchoring between the K-loop of kinesin and the C terminus of tubulin. *Proc. Natl Acad. Sci. USA* 97, 640–645 (2000).
39. Rogers, K. R. *et al.* KIF1D is a fast non-processive kinesin that demonstrates novel K-loop-dependent mechanochemistry. *EMBO J.* 20, 5101–5113 (2001).
40. Tucker, C. & Goldstein, L. S. B. Probing the kinesin-microtubule interaction. *J. Biol. Chem.* 272, 9481–9488 (1997).
41. Nogales, E., Wolf, S. G. & Downing, K. H. Structure of the αβ tubulin dimer by electron crystallography. *Nature* 391, 199–203 (1998).
42. Feynman, R. P. in *The Feynman Lectures on Physics* Vol. I (eds Feynman, R. P., Leighton, R. B. & Sands, M. L.) (Addison-Wesley, Reading, MA, 1963).
43. Oosawa, F. Sliding of actin filament on myosin and a flexible ratchet. *Jikeikai. Med. J.* 36, 219–231 (1989).
44. Vale, R. D. & Oosawa, F. Protein motors and Maxwell's demons: does mechanochemical transduction involve a thermal ratchet? *Adv. Biophys.* 26, 97–134 (1990).
45. Hirakawa, E., Higuchi, H. & Toyoshima, Y. Y. Processive movement of single 22S dynein molecules occurs only at low ATP concentrations. *Proc. Natl Acad. Sci. USA* 97, 2533–2537 (2000).
46. Kojima, H., Kikumoto, M., Sakakibara, H. & Oiwa, K. Mechanical properties of single-headed processive motor, inner-arm dynein subspecies-c of *Chlamydomonas* studied at the single molecule level. *J. Biol. Phys.* (in the press).

ACKNOWLEDGEMENTS

We thank Y. Ishii, F. Oosawa, Y. Inoue and colleagues of Single Molecule Processes Project, and Osaka University for discussions; J. West, E. Muto, H. Kojima and Y. Taniguchi for critically reading the manuscript. This work was partially supported by JSPS Research Fellowships for Young Scientists (M.N.). Correspondence and requests for materials should be addressed to H.H.

COMPETING FINANCIAL INTERESTS

The authors declare that they have no competing financial interests.

[CANCER RESEARCH 64, 4670–4676, July 1, 2004]

Estrogen-Related Receptor α in Human Breast Carcinoma as a Potent Prognostic Factor

Takashi Suzuki,[1] Yasuhiro Miki,[1] Takuya Moriya,[1] Norihiro Shimada,[1] Takanori Ishida,[2] Hisashi Hirakawa,[3] Noriaki Ohuchi,[2] and Hironobu Sasano[1]

Departments of [1]Pathology and [2]Surgery, Tohoku University School of Medicine, Sendai, Japan; and [3]Department of Surgery, Tohoku Kosai Hospital, Sendai, Japan

ABSTRACT

Estrogen-related receptor α (ERRα) was identified as a gene related to estrogen receptor α (ERα) and belongs to a class of nuclear orphan receptors. ERRα binds to estrogen responsive element(s) (ERE) and is considered to be involved in modulation of estrogenic actions. However, biological significance of ERRα remains largely unknown. Therefore, we examined the expression of ERRα in human breast carcinoma tissues using immunohistochemistry ($n = 102$) and real-time reverse transcription-PCR ($n = 30$). ERRα immunoreactivity was detected in the nuclei of carcinoma cells in 55% of breast cancers examined, and relative immunoreactivity of ERRα was significantly ($P = 0.0041$) associated with the mRNA level. Significant associations were detected between ERα and ERE-containing estrogen-responsive genes, such as pS2 ($P < 0.0001$) and EBAG9/RCAS1 ($P = 0.0214$), in breast carcinoma tissues. However, no significant association was detected between ERα and pS2 ($P = 0.1415$) in the ERRα-positive cases ($n = 56$) or between ERα and EBAG9/RCAS1 ($P = 0.8271$) in the ERRα-negative group ($n = 46$). ERRα immunoreactivity was significantly associated with an increased risk of recurrence and adverse clinical outcome by both uni- ($P = 0.0097$ and $P = 0.0053$, respectively) and multi- ($P = 0.0215$ and $P = 0.0118$, respectively) variate analyses. A similar tendency was also detected in the group of breast cancer patients who received tamoxifen therapy after surgery. Results from our study suggest that ERRα possibly modulates the expression of ERE-containing estrogen-responsive genes, and ERRα immunoreactivity is a potent prognostic factor in human breast carcinoma.

INTRODUCTION

Estrogens are well known to contribute immensely to the development of hormone-dependent breast carcinomas (1, 2). Biological effects of estrogens are mediated through an interaction with estrogen receptor (ER) α and/or β (3). ERs activate transcription of various target genes (*i.e.*, estrogen responsive genes) in a ligand-dependent manner by direct DNA interaction through the estrogen-responsive element(s) (ERE) or by tethering to other transcription factors (4, 5). Therefore, antiestrogens such as tamoxifen, which blocks ER, have been mainly used as an endocrine therapy in breast carcinoma for many years.

Estrogen-related receptor (ERR) family belongs to nuclear hormone receptors, and consists of three closely related members (α, β, and γ; Refs. 6 and 7). ERRs share significant homology to ERα at the DNA-binding domain and recognize the ERE (8–10), which indicates that ERRs modulate the actions of ERs (11–13). However, ERRs are not activated by known natural estrogens and are therefore classified as orphan receptors (14). ERRs can also bind to steroidgenic factor 1 (SF1)-binding element within the promoter regions of various steroidogenic P450 genes including aromatase (15, 16).

Previous *in vitro* studies have demonstrated the mRNA expression of ERRα in breast cancer cell lines (17) and breast carcinoma tissues (18). ERRα activated the expression of pS2, one of the estrogen responsive genes (17), in breast cancer cells, and it has also been reported that ERRα regulated aromatase expression in breast fibroblasts (11). However, a detailed examination of ERRα expression, including at the protein level, has not been examined in human breast carcinoma tissues, and the biological significance of ERRα remains largely unclear. Therefore, in this study, we examined the immunolocalization of ERRα in 102 cases of human breast carcinoma tissues and correlated these findings with various clinicopathological factors including the clinical outcome. In addition, we also examined mRNA expression of ERRα in 30 cases of breast carcinoma tissues using real-time reverse transcription-PCR and analyzed the correlation with the ERRα immunoreactivity or aromatase mRNA expression.

MATERIALS AND METHODS

Patients and Tissues. One hundred and two specimens of invasive ductal carcinoma of the breast were obtained from female patients who underwent mastectomy from 1985 to 1990 in the Department of Surgery, Tohoku University Hospital, Sendai, Japan. Breast tissue specimens were obtained from patients with a mean age of 53.6 years (range 27–82). None of the patients examined used oral contraceptives. The patients did not receive chemotherapy or irradiation before surgery. Eighty-eight patients received adjuvant chemotherapy, and ten patients received tamoxifen therapy after the surgery. The mean follow-up time was 106 months (range 4–157 months). The histological grade of each specimen was evaluated based on the method of Elston and Ellis (19). All specimens were fixed with 10% formalin and embedded in paraffin wax.

Thirty specimens of invasive ductal carcinoma were obtained from patients who underwent mastectomy in 2000 in the Departments of Surgery at Tohoku University Hospital and Tohoku Kosai Hospital, Sendai, Japan. Specimens of adipose tissue adjacent to the carcinoma and non-neoplastic breast tissues were available for examination in 7 and 5 of these 30 cases, respectively. Specimens for RNA isolation were snap-frozen and stored at −80°C, and those for immunohistochemistry were fixed with 10% formalin and embedded in paraffin-wax. Informed consent was obtained from all patients before their surgery and examination of specimens used in this study.

Research protocols for this study were approved by the Ethics Committee at both Tohoku University School of Medicine and Tohoku Kosai Hospital.

Antibodies. Mouse monoclonal antibody for ERRα (2ZH5844H) was purchased from Perseus Proteomics Inc. (Tokyo, Japan). This antibody was produced by immunizing mice with a systemic peptide corresponding to amino acids 98–171 of ERRα (GenBank accession number; X51416), and the characterization was confirmed by immunoblotting analyses.[4] Rabbit polyclonal antibody for estrogen sulfotransferase (EST; *SULT 1E1* gene; PV-P2237; Ref. 20) was purchased from Medical Biological Laboratory (Nagoya, Japan). EBAG9/RCAS1 antibody was a rabbit polyclonal antibody (21, 22) and was kindly provided from Dr. S. Inoue (Department of Biochemistry, Saitama Medical School, Saitama, Japan). Monoclonal antibodies for ERα (ER1D5), progesterone receptor (PR; MAB429), Ki-67 (MIB1), pS2 (M7184), cyclin D1 (P2D11F11), and c-myc (1–6E10) were purchased from Immunotech (Marseille, France), Chemicon (Temecula, CA), DAKO (Carpinteria, CA), DAKO, Novocastra Laboratories (Newcastle, United Kingdom), and Cambridge Research Biochemical (Cambridge, United Kingdom), respectively. Rabbit polyclonal antibodies for ERβ (06–629) and human epidermal growth factor

Received 1/26/04; revised 4/1/04; accepted 5/4/04.

The costs of publication of this article were defrayed in part by the payment of page charges. This article must therefore be hereby marked *advertisement* in accordance with 18 U.S.C. Section 1734 solely to indicate this fact.

Requests for reprints: Takashi Suzuki, Department of Pathology, Tohoku University School of Medicine, 2-1 Seiryo-machi, Aoba-ku, Sendai, 980-8575, Japan. Phone: 81-22-717-8050; Fax: 81-22-717-8051; E-mail: t-suzuki@patholo2.med.tohoku.ac.jp.

[4] Perseus Proteomics Inc., unpublished data.

receptor 2 (HER2; A0485) were obtained from Upstate Biotechnology (Lake Placid, NY) and DAKO, respectively.

Immunohistochemistry. A Histofine kit (Nichirei, Tokyo, Japan), which uses the streptavidin-biotin amplification method, was used for the identification of ERRα, ERα, PR, EST, HER2, Ki-67, pS2, EBAG9/RCAS1, cyclin D1, and c-myc immunoreactivity, whereas EnVision$^+$ (DAKO) was used for ERβ immunohistochemical analysis. Antigen retrieval for ERRα, ERα, ERβ, PR, HER2, Ki-67, EBAG9/RCAS1, and cyclin D1 immunostaining was performed by heating the slides in an autoclave at 120°C for 5 min in citric acid buffer [2 mM citric acid and 9 mM trisodium citrate dehydrate (pH 6.0)], and similarly, antigen retrieval for EST and pS2 immunostaining was done by heating the slides in a microwave oven for 15 min in a citric acid buffer. Dilutions of primary antibodies used in this study were as follows: ERRα, 1:1000; ERα, 1:50; ERβ, 1:50; PR, 1:30; EST, 1:9000; HER2, 1:200, Ki-67, 1:50; pS2, 1:30; EBAG9/RCAS1, 1:20; cyclin D1, 1:40; and c-myc 1:600. The antigen-antibody complex was visualized with 3,3'-diaminobenzidine solution (1 mM 3,3'-diaminobenzidine, 50 mM Tris-HCl buffer (pH 7.6), and 0.006% H_2O_2) and counterstained with hematoxylin.

Human tissues of heart were used as positive controls for ERRα immunohistochemistry (23). As a negative control for ERRα immunohistochemistry, normal mouse IgG was used instead of the primary antibody for ERRα, and no specific immunoreactivity was detected in these sections.

Real-Time Reverse Transcription-PCR. Total RNA was carefully extracted with guanidinium thiocyanate followed by ultracentrifugation in cesium chloride. A reverse transcription kit (SUPERSCRIPT II Preamplification system; Life Technologies, Inc., Grand Island, NY) was used in the synthesis of cDNA.

The Light Cycler System (Roche Diagnositics GmbH, Mannheim, Germany) was used to semi-quantify the mRNA level of ERRα, aromatase, and ribosomal protein L 13a (RPL13A) by real-time reverse transcription-PCR (24). Settings for the PCR thermal profile were as follos: initial denaturation at 95°C for 1 min followed by 40 amplification cycles of 95°C for 1 s, annealing at 62°C (ERRα), 60°C (aromatase), or 68°C (RPL13A) for 15 s, and elongation at 72°C for 15 s. The primer sequences used in this study are as follows: ERRα [X51416; forward 5'-TGCTCAAGGAGGGAGTGC-3' (cDNA position; 785–802) and reverse 5'-GGCGACAATTTCTGGTTCGGGTCAGGCATGGCATAG-3' (cDNA position; 981–998)], aromatase [(X13589; Ref. 20; forward 5'-GTGAAAAAGGGGACAAACAT-3' (cDNA position; 1286–1305) and reverse 5'-TGGAATCGTCTCAGAAGTGT-3' (cDNA position; 1481–1500)], and RPL13A [(NM012423; 25; forward 5'-CCTGGAGGAGAAGAGGAAAGAGA-3' (cDNA position; 487–509) and reverse 5'-TTGAGGACCTCTGTGTATTTGTCAA-3' (cDNA position; 588–612)]. Oligonucleotide primers for ERRα were designed in different exons to avoid the amplification of genomic DNA or human ERRα pseudo-gene (U85258). To verify amplification of the correct sequences, PCR products were purified and subjected to direct sequencing. Human heart tissue was used as a positive control for ERRα, whereas human placental tissue was used as a positive control for aromatase. Negative control experiments lacked cDNA substrate to check for the possibility of exogenous contaminant DNA, and no amplified products were detected under these conditions. mRNA level for ERRα and aromatase in each case has been summarized as a ratio of RPL13A and subsequently evaluated as a ratio (%) compared with that of the positive controls.

Scoring of Immunoreactivity and Statistical Analysis. ERRα, ERα, ERβ, PR, and Ki-67 immunoreactivity was scored in >1000 carcinoma cells for each case, and the percentage of immunoreactivity, *i.e.*, labeling index (LI), was determined. In this study, cases that were found to have ERRα LI of >10% were considered ERRα-positive breast carcinomas, according to a report for ERα and PR by Allred *et al.* (26). Immunoreactivity of EST was classified into the following three categories: ++, >50% positive cells; +, 1–50% positive cells; and −, no immunoreactivity, according to a previous report (20).

Values for LIs for ERRα, ERα, ERβ, PR, Ki-67, ERRα mRNA level, patient age, and tumor size were summarized as a mean ± 95% confidence interval. The association between immunoreactivity for ERRα status and these parameters were evaluated using a one-way ANOVA and Bonferroni test. The association between ERRα and PR LIs, and the association between ERRα mRNA and ERRα LI or aromatase mRNA were performed using a correlation coefficient (r) and regression equation. Statistical difference between ERRα status and menopausal status, stage, lymph node status, histological grade, ERα status, EST, or HER2 status was evaluated in a cross-table using the χ^2 test. Overall and disease-free survival curves were generated according to the Kaplan-Meier method, and the statistical significance was calculated using the log-rank test. Univariate and multivariate analyses were evaluated by Cox proportional hazards model using PROC PHREG in our SAS software. Differences with Ps < 0.05 were considered significant.

RESULTS

Immunohistochemistry for ERRα in Breast Carcinoma Tissues. Immunoreactivity for ERRα was detected in the nuclei of invasive ductal carcinoma cells (Fig. 1*A*). A mean value of ERRα LI in the 102 breast carcinoma tissues examined was 23.0% (range 0–75%), and a number of ERRα-positive breast carcinomas (*i.e.*, ERRα LI ≥ 10%) was 56 of102 cases (54.9%). ERRα immunoreactivity was focally detected in epithelial cells of morphologically normal glands (Fig. 1*B*), whereas the stroma or adipose tissue was immunohistochemically negative for ERRα. A mean value of ERRα LI in non-neoplastic mammary epithelia was 14.6% (range 0–33%), and the number of cases showing higher ERRα LI in carcinoma cells than that in non-neoplastic mammary epithelia was 49 of 102 (48.0%). In positive control sections for ERRα immunohistochemistry, ERRα immunoreactivity was markedly detected in the nuclei of myocardial cells of the heart (Fig. 1*C*).

Associations between ERRα immunoreactivity and clinicopathological parameters in 102 breast carcinomas are summarized in Table 1. ERRα immunoreactivity tended to be positively associated with ERα status and ERα LI and negatively associated with EST; however the correlation did not reach a statistical significance (P = 0.0848, P = 0.1485, and P = 0.1224, respectively). No significant association was detected between ERRα immunoreactivity and the other clinicopathological parameters examined, including patient age, menopausal status, stage, tumor size, lymph node status, histological grade, ERβ LI, PR LI, HER2 status, and Ki-67 LI, in this study.

Influence of ERRα Status on the Association between ERα and Estrogen Responsive Genes. pS2, EBAG9/RCAS1, PR, cyclin D1, and c-myc are all well recognized as estrogen-responsive genes in human breast cancers. As shown in Table 2, a significant positive association was detected between ERα LI and the status of these immunoreactivity genes except for c-myc in the 102 breast cancer tissues examined (P < 0.0001 for pS2, P = 0.0214 for EBAG9/RCAS1, P < 0.0001 for PR LI, P = 0.0002 for cyclin D1, and P = 0.9372 for c-myc), which agrees well with previous immunohistochemical studies (22, 27–30). However, when the breast cancers were classified into two groups according to ERRα status, no significant association was detected between ERα LI and pS2 in the group of ERRα-positive breast carcinomas (P = 0.1415; n = 56) or between ERα LI and EBAG9/RCAS1 in ERRα-negative breast cancers (P = 0.8271; n = 46). On the other hand, significant association was detected between ERα LI and PR LI (P < 0.0001 in ERRα-positive cases; P < 0.0001 in ERRα-negative cases) or cyclin D1 (P = 0.0126 in ERRα-positive cases; P = 0.0082 in ERRα-negative cases), regardless of the ERRα status in the breast cancer cases examined.

No significant association was detected between ERRα LI and these estrogen-responsive genes regardless of ERα status in 102 breast carcinoma tissues (Table 3).

Correlation between ERRα Immunoreactivity and the Clinical Outcome of the Patients. ERRα immunoreactivity was significantly associated with an increased risk of recurrence (P = 0.0071, log-rank test; Fig. 2*A*). After univariate analysis by Cox proportional hazards model (Table 4), lymph node status (P < 0.0001), tumor size (P < 0.0001), EST (P = 0.0035), and ERRα immunoreactivity

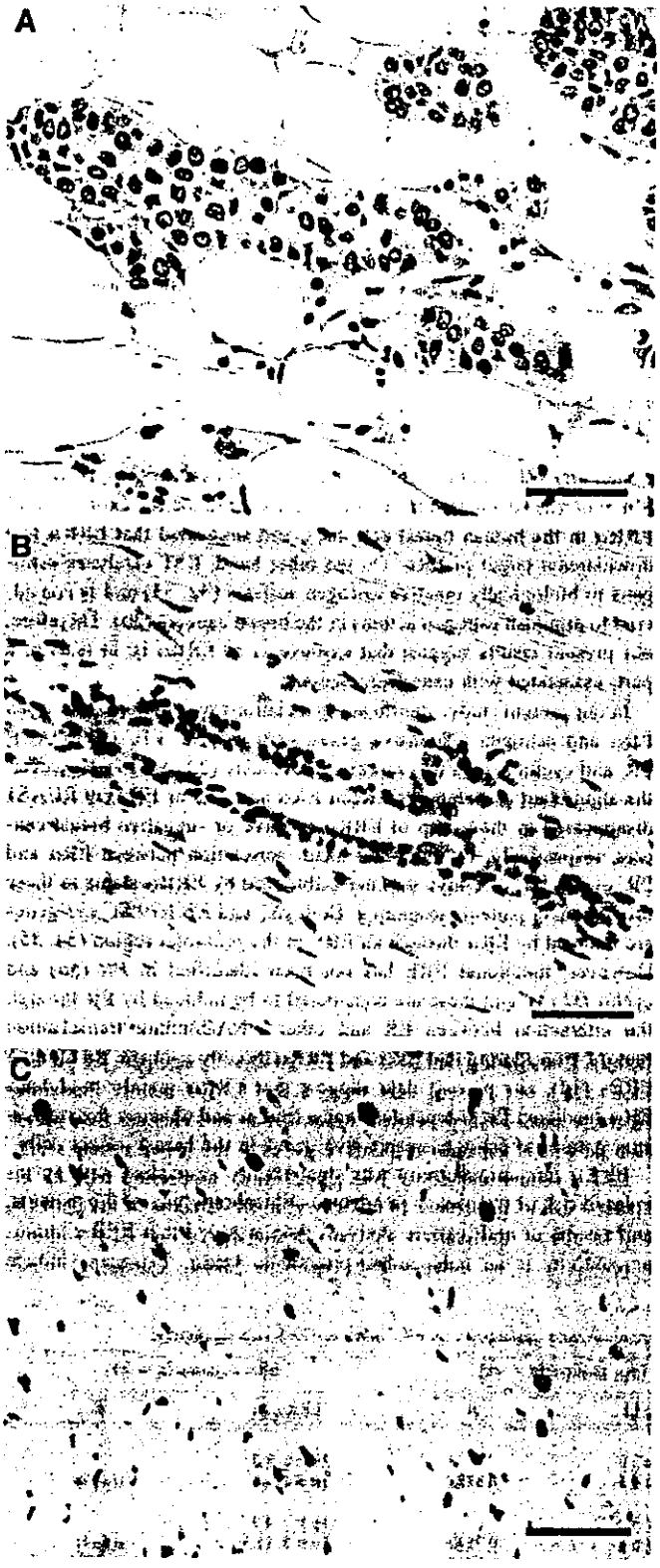

Fig. 1. Immunohistochemistry for ERRα in invasive ductal carcinoma. *A*, ERRα immunoreactivity was detected in the nuclei of invasive ductal carcinoma cells. *ERR*, estrogen-related receptor α. *B*, in morphologically normal mammary glands, immunoreactivity for ERRα was weakly detected in the nuclei of epithelial cells. *C*, in the positive control for ERRα immunohistochemistry, ERRα immunoreactivity was detected in the nucleus of myocardial cells in the heart. *Bar* = 50 μm, respectively.

Table 1 *Association between ERRα immunoreactivity and clinicopathological parameters in 102 breast carcinomas*

	ERRα immunoreactivity		
	+ (n = 56)	− (n = 46)	P
Age (yrs)[b]	54.3 ± 1.6	52.8 ± 1.8	0.5271
Menopausal status			
Premenopausal	27 (26.5%)	20 (19.7%)	
Postmenopausal	29 (28.4%)	26 (25.5%)	0.6329
Stage			
I	14 (13.7%)	15 (14.7%)	
II	35 (34.3%)	26 (25.5%)	
III	7 (6.9%)	5 (4.9%)	0.6852
Tumor size (mm)[b]	25.6 ± 1.8	24.8 ± 1.8	0.7443
Lymph node status			
Positive	27 (26.5%)	19 (18.7%)	
Negative	29 (28.4%)	27 (26.5%)	0.4849
Histological grade			
1	14 (13.7%)	13 (12.7%)	
2	22 (21.6%)	14 (13.7%)	
3	20 (19.7%)	19 (18.6%)	0.6462
ERα status			
Positive	45 (44.1%)	30 (29.4%)	
Negative	11 (10.8%)	16 (15.7%)	0.0848
ERα LI[b]	47.5 ± 4.5	38.1 ± 5.2	0.1485
ERβ LI[b]	15.3 ± 2.4	14.6 ± 2.7	0.8493
PR LI[b]	45.6 ± 4.8	40.7 ± 5.1	0.4894
EST			
−	35 (34.3%)	24 (23.5%)	
+	10 (9.8%)	15 (14.7%)	
++	11 (10.8%)	7 (6.9%)	0.1224
HER2 status			
Positive	20 (19.6%)	15 (14.7%)	
Negative	36 (35.3%)	31 (30.4%)	0.7421
Ki-67 LI[b]	24.7 ± 2.0	27.4 ± 2.7	0.4045

[a] ERRα, estrogen-related receptor α; ERα, estrogen receptor α; LI, labeling index; EST, estrogen sulfotransferase; HER2, human epidermal growth receptor 2.
[b] Data are presented as mean ± 95% confidence interval. All other values represent the number of cases and percentage.

(P = 0.0097) were demonstrated as significant prognostic parameters for disease-free survival in 102 breast carcinoma patients. A multivariate analysis (Table 4), however, revealed that only lymph node status (P = 0.0015) and ERRα immunoreactivity (P = 0.0215) were independent-prognostic factors with relative risks over 1.0, whereas tumor size and EST were not significant.

Overall survival curve was demonstrated in Fig. 2*B*, and a significant correlation was detected between ERRα immunoreactivity and adverse clinical outcome of the patients (P = 0.0018, log-rank test). Using a univariate analysis (Table 5), lymph node status (P < 0.0001), tumor size (P = 0.0002), ERRα immunoreactivity (P = 0.0053), EST (P = 0.0065), HER2 status (P = 0.0175), adjuvant chemotherapy (P = 0.0233), and histological grade (P = 0.0310) turned out to be significant prognostic factors for overall survival in this study. Multivariate analysis revealed that lymph node status (P = 0.0085), ERRα immunoreactivity (P = 0.0118), and EST (P = 0.0382) were independent-prognostic factors with a relative risk over 1.0; however other factors were not significant in this study (Table 5).

Ten patients received tamoxifen therapy after surgery, and these cases were ERα-positive breast cancers. The disease-free and overall survival curves in these patients were summarized in Fig. 2, *C* and *D*. ERRα immunoreactivity was also markedly associated with an increased risk of recurrence and worse prognosis in the group of breast cancer patients who received tamoxifen therapy, although *P*s were not available because no patient had a recurrence or died in the group of ERRα-negative breast cancers. Association between ERRα immunoreactivity and clinical outcome of the patients was not significantly changed regardless of the status of adjuvant chemotherapy after surgery in this study (data not shown).

Table 2 *Correlation between ERα[a] and estrogen responsive gene immunoreactivities associated with ERRα status in 102 breast carcinomas*

	Total (n = 102)		ERRα positive (n = 56)		ERRα negative (n = 46)	
	ERα LI	P	ERα LI	P	ERα LI	P
pS2						
Positive	54.7 ± 4.0		54.3 ± 5.5		53.8 ± 6.5	
Negative	28.8 ± 5.1	**<0.0001**	38.5 ± 7.2	0.1415	14.8 ± 6.3	**<0.0001**
EBAG9/RCAS1						
Positive	46.7 ± 4.4		51.6 ± 5.9		40.8 ± 6.7	
Negative	27.9 ± 7.3	**0.0214**	17.4 ± 6.1	**0.0093**	45.0 ± 16.4	0.8271
PR LI		**<0.0001**		**<0.0001**		**<0.0001**
		(r = 0.590)		(r = 0.515)		(r = 0.675)
Cyclin D1						
Positive	57.3 ± 4.5		59.6 ± 6.0		54.5 ± 7.0	
Negative	32.2 ± 4.4	**0.0002**	37.2 ± 6.0	**0.0126**	26.5 ± 6.5	**0.0082**
c-myc						
Positive	43.7 ± 5.3		47.9 ± 6.8		37.4 ± 8.3	
Negative	44.2 ± 4.5	0.9372	48.4 ± 6.1	0.9583	39.8 ± 6.7	0.8321

Ps < 0.05 were considered significant, and described as boldface.
[a] ERα, estrogen receptor α; ERRα, estrogen-related receptor α; PR, progesterone receptor; LI, labeling index.

ERRα mRNA Expression in the Breast Carcinoma Tissues. mRNA expression for ERRα, aromatase, and RPL13A was detected as a specific single band (214, 215, and 126 bp, respectively) and was semi-quantified by real-time reverse transcription-PCR. Expression of ERRα mRNA was detected markedly in the breast carcinoma tissues (65.7 ± 9.0%) but was low in non-neoplastic breast tissues (25.4 ± 6.0%, P = 0.0448 *versus* carcinoma tissues) or adipose tissues adjacent to the carcinoma (12.6 ± 7.3%, P = 0.0174 *versus* carcinoma tissues; Fig. 3*A*). ERRα mRNA expression was closely correlated with the ERRα immunoreactivity evaluated as ERRα LI (P = 0.0041, r = 0.509) in 30 breast carcinoma tissues examined (Fig. 3*B*). However, mRNA expression of ERRα was not significantly associated with that of aromatase (P = 0.6441, r = -0.088) in this study (Fig. 3*C*).

DISCUSSION

In this study, ERRα immunoreactivity was detected in the nuclei of carcinoma cells in 55% of breast cancer tissues and was significantly associated with its mRNA level. ERRα mRNA expression was demonstrated previously in various human breast cancer cell lines, breast carcinoma tissues, and normal mammary epithelial cells (17, 18), and our present findings were in good agreement with these previous reports. Results in our present study also demonstrated that ERRα immunoreactivity tended to be positively or inversely associated with ERα or EST, respectively. The possible correlation between ERRα and ERα expression remains controversial. Ariazi *et al.* (18) reported that increased ERRα mRNA levels were associated with ER-negative and PR-negative tumor status in 38 breast cancer tissues and suggested a possible unfavorable marker in the breast cancers. However, Liu *et al.* (31) demonstrated that estrogens stimulate the expression of ERRα in the human breast cell lines, and suggested that ERRα is a downstream target of ERα. On the other hand, EST catalyzes estrogens to biologically inactive estrogen sulfates (32, 33) and is considered to diminish estrogen actions in the breast cancers (20). Therefore, our present results suggest that expression of ERRα is, at least in a part, associated with estrogenic actions.

In our present study, significant associations were detected between ERα and estrogen responsive genes such as pS2, EBAG9/RCAS1, PR, and cyclin D1, as was reported previously (22, 27–29). However, the significant association between ERα and pS2 or EBAG9/RCAS1 disappeared in the group of ERRα-positive or -negative breast cancers, respectively. On the other hand, correlation between ERα and PR, cyclin D1, or c-myc was not influenced by ERRα status in these breast cancer patients examined. Both *pS2* and *EBAG9/RCAS1* genes are induced by ERα through an ERE in the promoter region (34, 35). However, functional ERE has not been identified in *PR* (36) and *cyclin D1* (5), and these are considered to be induced by ER through the interaction between ER and other DNA-binding transcription factors. Considering that ERα and ERRα directly compete for binding EREs (13), our present data suggest that ERRα mainly modulates ERα-mediated ERE-dependent transcription and changes the expression pattern of estrogen-responsive genes in the breast cancer cells.

ERRα immunoreactivity was significantly associated with an increased risk of recurrence or adverse clinical outcome of the patients, and results of multivariate analyses demonstrated that ERRα immunoreactivity is an independent-prognostic factor. Estrogens induce

Table 3 *Correlation between ERRα[a] and estrogen responsive gene immunoreactivities associated with ERα status in 102 breast carcinomas*

	Total (n = 102)		ERα positive (n = 75)		ERα negative (n = 27)	
	ERRα LI	P	ERRα LI	P	ERRα LI	P
pS2						
Positive	23.5 ± 2.7		23.0 ± 2.9		27.7 ± 8.6	
Negative	22.4 ± 3.4	0.7981	27.7 ± 4.5	0.3777	16.3 ± 4.8	0.2776
EBAG9/RCAS1						
Positive	22.6 ± 2.6		24.2 ± 3.0		18.5 ± 4.9	
Negative	23.6 ± 5.8	0.8834	21.8 ± 6.8	0.7542	29.0 ± 11.3	0.5341
PR LI		0.5072		0.9069		0.9671
		(r = 0.066)		(r = 0.014)		(r = 0.008)
Cyclin D1						
Positive	24.7 ± 3.4		24.8 ± 3.6		23.3 ± 11.0	
Negative	21.8 ± 2.8	0.5134	24.2 ± 3.4	0.9058	18.1 ± 4.7	0.6770
c-myc						
Positive	25.0 ± 3.3		25.8 ± 3.7		22.5 ± 7.7	
Negative	22.0 ± 2.8	0.4943	23.7 ± 3.4	0.6648	17.8 ± 5.3	0.6100

[a] ERRα, estrogen-related receptor α; LI, labeling index; ERα, estrogen receptor α; PR, progesterone receptor.

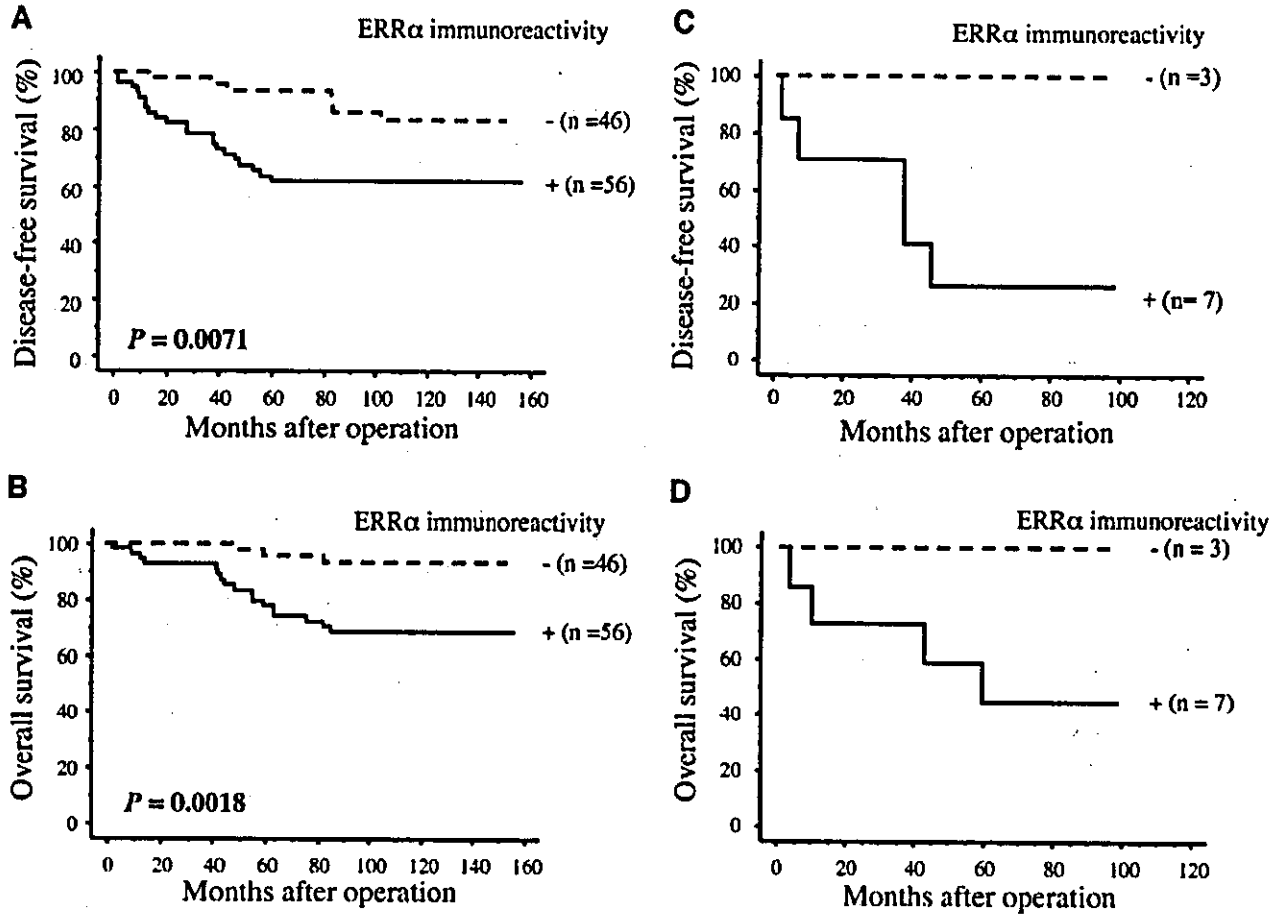

Fig. 2. *A* and *B*, disease-free (*A*) and overall (*B*) survival of 102 patients with breast carcinoma according to ERRα immunoreactivity (Kaplan-Meier method). ERRα immunoreactivity was significantly associated with an increased risk of recurrence ($P = 0.0071$, log-rank test; *A*, and worse prognosis ($P = 0.0018$, log-rank test). *C* and *D*, disease-free (*C*) and overall (*D*) survival of 10 patients received tamoxifen therapy after surgery according to ERRα immunoreactivity (Kaplan-Meier method). ERRα immunoreactivity was also associated with an increased risk of recurrence (*C*) and worse prognosis (*D*) in the group of patients who received tamoxifen therapy. *Ps* were not calculated, because no patient had a recurrence or died in the group of ERRα-negative breast cancer patients. *ERR*, estrogen-related receptor α.

Table 4 *Univariate and multivariate analyses of disease-free survival in 102 breast cancer patients examined*

Variable	*P*		Relative risk (95% CI[a])
	Univariate	Multivariate	
Lymph node status (pN_3-pN_0)[b]	<0.0001[c]	0.0015	2.593 (1.441–4.666)
Tumor size (75–7 mm)[b]	<0.0001[c]	0.3306	
EST (−/+, ++)	0.0035[c]	0.0613	
ERRα immunoreactivity (positive/negative)	0.0097[c]	0.0215	1.953 (1.116–3.149)
c-myc (positive/negative)	0.0581		
Adjuvant chemotherapy (no/yes)	0.1305		
Ki-67 LI (≥10/<10)	0.1795		
HER2 status (positive/negative)	0.2713		
Histological grade (3/1, 2)	0.2911		
ERα status (positive/negative)	0.4363		

[a] CI, confidence interval; EST, estrogen sulfotransferase; ERRα, estrogen-related receptor α; HER2, human epidermal growth factor receptor 2; LI, labeling index; ERα, estrogen receptor α.

[b] Data were evaluated as continuous variables in the uni- and multivariate analyses. All other data were evaluated as dichotomized variables.

[c] Data were considered significant in the univariate analyses, and were examined in the multivariate analyses.

various estrogen responsive genes in breast cancer cells, and these genes include not only activators of cell growth such as cyclin D1 (37) or c-myc (38) but also relatively good prognostic markers such as pS2 (29) or PR (39). ERRs display significant constitutive transcriptional activity (7, 9, 40). Therefore, poor clinical outcome in ERRα-positive breast cancer patients may be partly caused by constitutive modulation of the expression of estrogen-responsive genes, although we could not directly demonstrate such hypothesis from our present data, because of the lack of mechanistic examinations and the relatively limited number of cases examined in this study. Additional examinations are required to clarify the detailed mechanism of ERRα action in the breast cancer tissues.

Table 5 *Univariate and multivariate analyses of overall survival in 102 breast cancer patients examined*

Variable	*P*		Relative risk (95% CI[a])
	Univariate	Multivariate	
Lymph node status (pN_3-pN_0)[b]	<0.0001[c]	0.0085	2.414 (1.252–4.653)
Tumor size (75–7 mm)[b]	0.0002[c]	0.2675	
ERRα immunoreactivity (positive/negative)	0.0053[c]	0.0118	5.076 (1.217–21.173)
EST (−/+, ++)	0.0065[c]	0.0382	4.101 (1.027–19.705)
HER2 status (positive/negative)	0.0175[c]	0.4669	
Adjuvant chemotherapy (no/yes)	0.0233[c]	0.0635	
Histological grade (3/1, 2)	0.0310[c]	0.1458	
Ki-67 LI (≥10/<10)	0.1818		
c-myc (positive/negative)	0.2697		
ERα status (positive/negative)	0.7646		

[a] CI, confidence interval; ERRα, estrogen-related receptor α; EST, estrogen sulfotransferase; HER2, human epidermal growth factor receptor 2; LI, labeling index; ERα, estrogen receptor α.

[b] Data were evaluated as continuous variables in the uni- and multivariate analyses. All other data were evaluated as dichotomized variables.

[c] Data were considered significant in the univariate analyses, and were examined in the multivariate analyses.